Design of Low Airflow Sensor to Measure Airflow Close to Plant Leaf

Saurabh Lavaniya

Integrated Devices and Systems (IDS)

Electrical Engineering, Mathematics and Computer Science

University of Twente

March 2020

Supervisors

dr.ir.R.J.WIEGERINK

dr.ir.T.E.VAN DEN BERG

Abstract

The thesis is part of a bigger project "Plantenna" which is a collaboration of 4 universities. The thesis aims to investigate different types of sensors and designs capable of measuring low airflows (< 1 m/s). The most suitable sensor is designed to measure airflow near the leaf. The challenge is to design a sensor which can measure the airflow without disturbing the crucial parameters like temperature, humidity, and flow itself.

The drag force based flow sensor is modeled and simulated in COMSOL Multiphysics 5.5 and verified by analytical model and finally, fabricated in $MESA^+$ lab at University of Twente. To characterize the sensor, a test setup is constructed. Velocity profile in the test setup is recorded with Voltcraft's PL-135 anemometer sensor to characterize the fabricated flow sensor.

Acknowledgement

This Thesis is final research project carried out to obtain Master's degree in Electrical Engineering (Integrated Devices and Systems) at the University of Twente.

I would like to express my sincere gratitude towards dr.ir.R.J.Wiegerink for your patience and guidance throughout the project. Nevertheless, corona virus made things more challenging, but you kept me motivated through the tough time. I could not have finished this project without his constant support and help. I would like to thank dr.ir.T.E.Vandenberg for having faith in me and helping out whenever asked. I would like to thank R.PJ. Sanders who sat with me the whole day to help me do measurement at the end days.

I would like to thank dr.ir.Dennis Alveringh and the whole team for brain storming sessions on mask designing and fabrication

Contents

Chapter 1: Introduction

1.1 Background on Horticulture and Greenhouse

Horticulture consists of two parts *Hortus*: means garden and *colere*: means to grow and cultivate (culture means cultivation). Horticulture is the science and art of the development, sustainable production, marketing, and use of high-value, intensively cultivated food and ornamental plants [1]. Plants grown by this science are diverse, which include annual and perennial species, fruits and vegetables, and decorative indoor and landscape plants. There is a direct relationship between horticulture and science.

Crop Science also called agronomy, is the science of producing the world's major food groups, grain, feed, turf, and fiber crops, and incorporates production, improvement, and marketing [2].On the other hand, botany is the academic study of plants and does not incorporate the applications of plant use, improvement, or marketing. Horticulture is an application science – the science developed by horticulturists is applied to plant production, improvement, marketing, and the enhancement of Earth's human and animal life.

From a nutrition point of view, horticulture is most important because the human body needs nutrition to carry with its day-to-day life. It enables us to produce fruits and vegetables out of seasons with better care and more production. Without a doubt, horticulture can be used to increase the production of the crop, generate employment, improving economic conditions for farmers and entrepreneurs, and enhancing exports In 2018, horticultural contributed 21.1 billion euros to the Dutch economy, which is 2.7 percent of the Netherlands' gross domestic product (GDP) [3].

To provide a conducive growing atmosphere to plants, Greenhouses are employed for controlled growth and environment. Oxford Dictionary defines a *greenhouse* (also called a glasshouse, or, if with sufficient heating, a hothouse) as a structure with walls and roof made of transparent material, such as glass, in which plants requiring regulated climatic conditions are grown. These structures' sizes range from small shed to industrial-sized buildings. Figure 1 shows an industrial-sized greenhouse [4]

Figure 1: Image of a greenhouse [4]

A large number of commercial glasshouses are equipped with high-tech production facilities for growing vegetables, flowers, and fruits. A typical Industrial glasshouse is equipped with advanced technical tools for ventilation, cooling, heating, lighting, screening installations and, may be controlled by a computer to optimize the conditions, such as air temperature, pressure, the relative humidity for optimum plant growth. In a cold climate, it is a great advantage of having a controlled environment, on the other hand, for moderate and tropical regions, it can provide an extension in the production season and protection against diseases and insects. If properly managed, it can significantly increase crop quality and yield. Generally, the cost of the crop coming from the greenhouse is higher, due to initial investments in structure, energy, and pieces of equipment. But the cost can be effectively monitored by the understanding of optimal micro-climate parameters to achieve a higher yield at low expenses.

Most of the energy requirement goes into the heating and cooling of the greenhouses. Thus, reducing excessive energy requirements should be the key concern to maintain a competitive price in the market. For example, tomato is sensitive to both cold and hot climates, cultivating them in such a climate will require additional risk and production cost [5]. Thus, here is a sustainability challenge to shift from energy-consuming to energyneutral greenhouses. This can be done by critically studying how far one can go from the optimal micro-climate, without sacrificing the yield and quality of the crop.

The main environmental factors affecting the greenhouse climate include airflow and root-zone temperatures, relative humidity, light conditions, disease, and insect intervention, as well as carbon dioxide concentration. These parameters are known to influence the growth, transpiration process, and physiological cycles such as photosynthesis and respiration in plants. A detailed study on the effect of such parameters on processes like transpiration could help in the efficient management of greenhouse climate control and cost-effective all-year cultivation. For example, studying a particular plant's behavior with variation in temperature, humidity, airflow, and light intensity in a laboratory could help in gaining a better understanding of these physiological processes that, in turn, could help in increasing yield and saving energy. This thesis will be focused on airflow and its influence on growth or biological processes in plants.

Figure 2: HAF system in a greenhouse [7]

Nowadays, HAF (horizontal airflow) systems are being employed in the greenhouse together with natural ventilation [6]. A typical example is shown in Figure 2 [7]. The HAF concept utilizes the principle that air that moves in a coherent horizontal pattern in a building like a greenhouse needs only enough energy to overcome turbulence and friction loss to keep it moving [8]. The airflow system helps to reduce micro-climate heterogeneity (temperature, humidity, and CO_2) inside the greenhouse. This is one of the key factors for uniform growth.

One of the biological processes which are affected by airflow is Transpiration, which is the loss of water vapors from the plants, is a physical process that is controlled by both external physical and physiological factors [9]. Solar radiation is a major source of energy for transpiration. The rate of transpiration is proportional to the gradient of water vapor concentration between the source (within plants) and the sink (atmosphere) and, proportional to the resistance to vapor diffusion of the plant. The major water loss happens through leaves via stomata, which largely control the leaf transpiration. The opening and closing of stomata are rather complex, depending on environmental factors such as light, humidity, temperature, CO_2 concentration, and endogenous factors such as root and leaf hormone production and release, and age [9].

The resistance to vapor diffusion depends on the air layer adjacent to the leaf surface, the so-called boundary layer (BL). It represents a region from the surface of the leaf to a point where the wind speed is negligibly affected by the surface friction. The airflow in the BL can be laminar or turbulent. Heat and mass are transferred through this layer through molecular diffusion (conduction). Resistance to such exchange via BL can be represented as Boundary Layer Resistance (BLR). The magnitude of this resistance depends on the depth of the BL and the size of the leaf. A thick BL can obstruct the transfer of heat and CO_2 and water vapors from the leaf to the environment.

It is essential to study the factors that influence the BL, especially in a controlled production environment like a greenhouse. Several factors influence the BL thickness including characteristics of leaves. Leaves that are larger (in size) and have pubescence or hair typically have a thicker boundary layer. A dense canopy (In biology, the canopy is the spatial arrangement of the aboveground portion of a plant, formed by the collection of individual plant crowns with very tight spacing [10][11], see Figure 3 for example) can hinder the air movement and increase the BL thickness. The thickness δ of laminar a BL at a distance x from the upwind edge of a flat plate can be expressed by the following semi-empirical expression [12].

$$\delta = \sqrt{\frac{\upsilon x}{u}} \tag{1.1}$$

Where υ is the kinematics viscosity of air and u is the wind speed. The δ is inversely proportional to the wind speed. Thus, it is one of the important factors that largely influence the boundary layer thickness. That is why it is advised to have adequate air movement inside the greenhouses. Inside a greenhouse with inadequate and horizontal airflows from fans, the BL can be thick enough to impede photosynthesis and environmental exchange of heat and mass, thus the growth of the plant.

The boundary layer (BL) can be considered as a micro-climate that surrounds the leaf and the growing points of the plants [13]. In case of no air movement or dense canopy, the BL is thick, the micro-climate around the leaves becomes increasingly different from the surrounding air. In other words, the temperature and the relative humidity can become high, reducing the water loss (transpiration) from plants. The concentration of the CO_2 can also drop down if the consumption of the CO_2 for photosynthesis is faster than the replenishment from the surrounding air [8]. Due to the reduction in transpiration from the leaves, water uptake from the soil through the plants also diminishes. This could result in nutrition deficiencies and hamper plant growth.

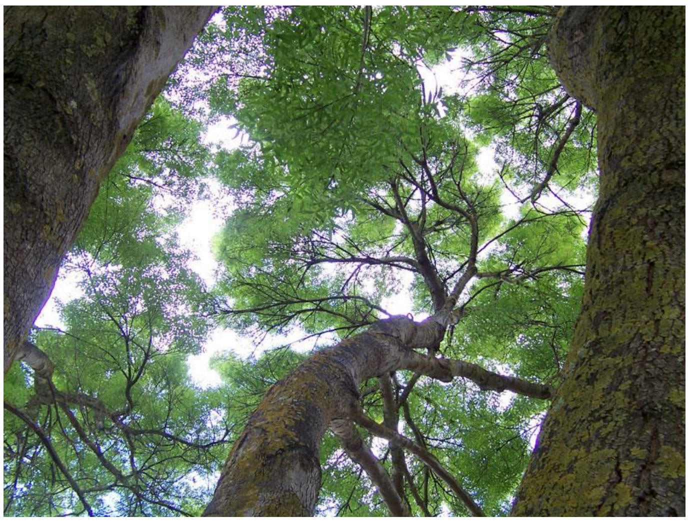

Figure 3: Canopy of the deciduous forest [5]

The easy solution one can think of is to have greenhouses with ventilation and horizontal fans for the movement of air. In large-size industrial greenhouses, the air movement can be energy-consuming and increase the input cost of production. Hence, the study of air movement or boundary layer to predict the minimum airflow at the different parts of the canopy in the greenhouses is critical.

In this report, flow sensors will be investigated, and a flow sensor will be designed to measure the wind-speed at different parts of the canopy to estimate the thickness of BL and make the study of important concepts like boundary layer conductance easier for the biologists. The horizontal airflow in the greenhouse depends on the size of the greenhouse, produced crop, its arrangement, and many other factors. Thus, a flow of 1 m/s boundary layer of a leaf can be estimated by equation *1.1*. Note that equation *1.1* is valid over a flat plate. Since the leaf is not flat, the result will differ from the actual measurements. Hence, the boundary layer thickness for $x = 1\,mm, u = 1 m/s\ and, v = 1.81 \times 10^{-5}\ kg/ms^{-1}$ estimated to be $1.3 \times 10^{-4} m$.

1.2 Aim of the Thesis

The Thesis is a part of the bigger project called "Plantenna" which is currently going on in-collaboration with 4TU ((TU Delft, Eindhoven University of Technology, University of Twente, and the University of Wageningen). The mission of Plantenna is to develop vegetation-integrated, energy harvesting, autonomous sensors that measure in-plant and environmental parameters at high resolution, and low cost [14]. The idea is to use the information from the sensors to develop the methods for early detection of plant stress and environmental strain. Finally, these methods shall help optimize water and nutrient application schemes for climate-smart agriculture, improve drought protection, and strengthen the decision-making for environmental protection and climate resilience.

The thesis aims to investigate the available sensors which are capable of detecting airflow up to 1 m/s (max) near the leaf. The challenge is to measure the airflow without disturbing the crucial parameters like temperature, humidity, and flow itself near the leaf. Sensor information can be used to estimate the thickness of the boundary layer. For the measurement of velocity near the leaf, the sensor could be mounted on one end of a probe, with the other part fixed to the microscope (see Figure 4)

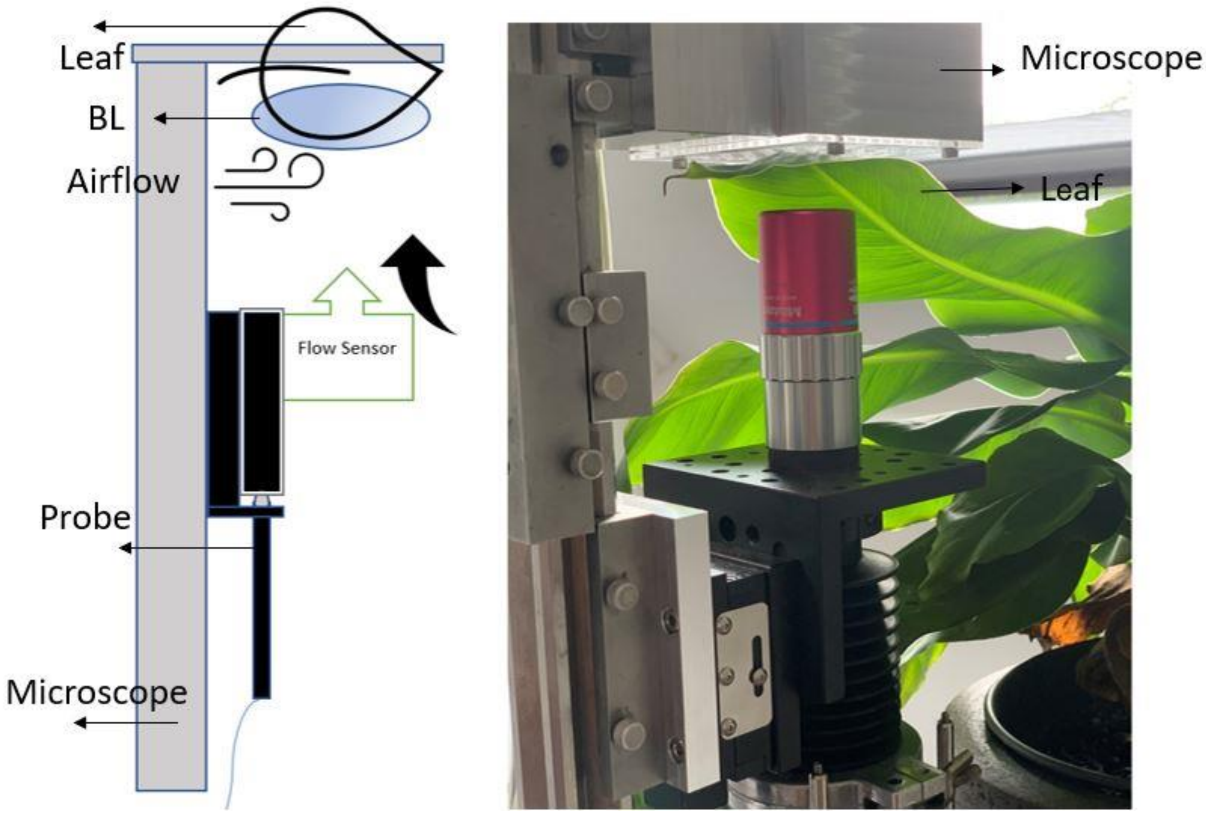

Figure 4: An idea for an experimental setup for flow measurement

The microscope can move along the z-axis with 1µm precision. The sensor will collect the flow information with each step near the leaf. Later, the information can be compiled to approximately evaluate the boundary layer thickness.

The measurement requirements put many limitations on the sensor itself, such as the size of the sensor should be as low as possible. A larger size or area of the sensor may hinder or change the flow near the leaf. Hence, the area of the sensor in contact with the flow should be small enough that it negligibly affects the airflow. The sensor should be very sensitive to measure such a low flow. If such measurement is not possible with available sensors then, a sensor capable to measure flow in the given situation shall be designed and fabricated. Measurements on the fabricated device could be carried out if falls within the time duration of the thesis.

1.3 Structure of the Thesis

The Thesis has been divided into 6 chapters as follows:

Chapter 1 provides background on Horticulture and Greenhouses and motivation to measure the flow near the leaf followed by the structure of the thesis.

Chapter 2 consists of the literature review on the investigated sensors and motivation to choose the final sensor or the design of the sensor to carry out such measurements.

Chapter 3 explains the design and modeling of the flow sensor which includes the mathematical calculations and simulations for the design of the sensor.

Chapter 4 explains the Mask designing for the MEMS Fabrication process.

Chapter 5 is dedicated to the electronics to convert the flow information from the flow sensor into the desired output form.

Chapter 6 covers the measurement results and the characterization of the flow sensor.

Chapter 2: Literature Review

In this chapter, the available sensors in the market will be investigated to figure out which sensor or which design could be best suitable to perform airflow measurements near a leaf.

2.1 Thermal Flow Sensors

Thermal flow sensors utilize the natural phenomenon of convection in which heat is transferred to the flowing fluid that, in turn, is converted to an electrical signal. The variation in the electrical signal conveys the response of the sensor to the flow change. To limit the heat transfer only due to flow, the sensors should ideally be thermally isolated. This means the loss of heat due to the other pathways such as through substrate or electrical contacts should be minimized to avoid performance degradation of the sensor. With thermal flow sensors, high accuracy and sensitivity can be achieved with low signal drift at the output. These sensors also provide a great advantage as they can sense without the need for any mechanically moving micro-components [15]. Generally, a thermal sensor consists of two parts: heater and sensing element. Sensing elements are placed to detect the heat transfer between the heaters and the flowing fluid, and its variation with the flow velocity. Thus, sensitivity could be improved if more heat is transferred to the fluid in comparison with the other pathways for heat to transfer.

Three types of thermal flow sensors can be seen in the literature [16]:

- Hot-wire and Hot-film or Anemometers
- Calorimetric
- Time of Flight

2.1.1 Hot- wire or Hot-Film (H-shape)

Hot-wire or hot-film sensor works on the principle of heat transfer from a heated element to a fluid that is cooler than the element. The term hot-wire or hot-film can be thought of as a resistive (electrical) element placed in the flow. Regardless of their different form, they have the same physical sensing principle. The resistive element is heated and subjected to fluid flow. The heat is transferred to fluid due to convective losses.

Figure 5 illustrates the working of the hot-wire anemometry [17]. As the flow increases the convective losses increase from the heated element, which means heat loss is a measure for the flowrate. The resistive element will experience a change in electrical resistance based upon the temperature change. Thus, the heat transfer rate can be converted into an electrical signal dependent on flow.

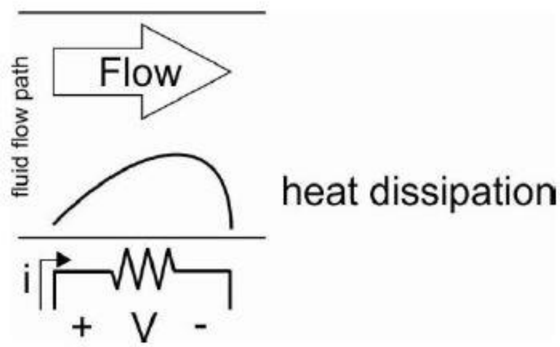

Figure 5: Schematic illustrating the working of Hot-wire [17]

According to King's law [18], the heat transfer is a function of fluid velocity given by:

$$Q_h = \mathrm{a} + \mathrm{bv}^{\mathrm{n}} \qquad 2.1$$

Where Q_h = heat dissipated,

v = fluid velocity and,

a, b, n are constants depending on thermal properties and flow geometry that are evaluated empirically [17]

For a typical thermal sensor material, the relationship between the resistance and temperature is given by:

$$R(T) = R(T_0)[1 + \alpha(\Delta T)] \qquad 2.2$$

Where $R(T)$ is the resistance at temperature T,

α is TCR (Temperature coefficient of resistivity) and,

T_0 is reference temperature

High TCR for the hot-wire material is recommended. As can be seen from equation *2.2*, the higher the TCR more variation in the resistance at a constant temperature can be achieved. Higher resistivity or higher resistance at reference temperature will also increase the sensitivity. The chosen material should have resistance such that it is easy to heat up with electrical current at practical voltages [19]. Platinum is one of the most common materials used for the thermal flow sensor. Though platinum does not have the highest TCR (refer to Table 1). But its corrosion-resistant property, high operating temperature range, and compatibility with existing micromachining technology make it a wonderful material for thermal flow sensing. Table 1 shows the electrical and thermal properties of a few commonly used materials in thermal flow sensing [20].

Table 1:Electrical and Thermal properties of materials for thermal flow sensor [18]

Material	Resistivity, ρ (Ω-m) at 20° C	TCR, α $(10^{-4}/K)$
Aluminum	2.69×10^{-8}	42.0
Copper	1.67×10^{-8}	43.0
Gold	2.30×10^{-8}	39.0
Iron	9.71×10^{-8}	65.1
Nickel	6.84×10^{-8}	68.1
palladium	10.8×10^{-8}	37.7
Platinum	10.6×10^{-8}	39.2
silver	1.63×10^{-8}	41.0
Tungsten	5.50×10^{-8}	46.0

The anemometer can be operated in two modes based upon heat dissipation: constant temperature or constant power [21]. In constant power mode, a constant power is supplied to the element and the temperature is monitored as the fluid passes through the element.

$$P = I^2 \times R \propto Q_h \tag{2.3}$$

However, constant temperature mode requires a feedback loop to maintain the constant temperature, and the extra power required to maintain the temperature is monitored. Despite complex implementation, constant temperature can produce better sensor resolution and frequency response [20].

2.1.2 Calorimetric flow sensors

Calorimetric is a mass flow sensor, works on the principle of heat transfer to a fluid via convection when placed in a flow. Generally, it comprises a heater and two sensing elements placed symmetrically upstream and downstream with respect heater (see Figure 6 [22]).

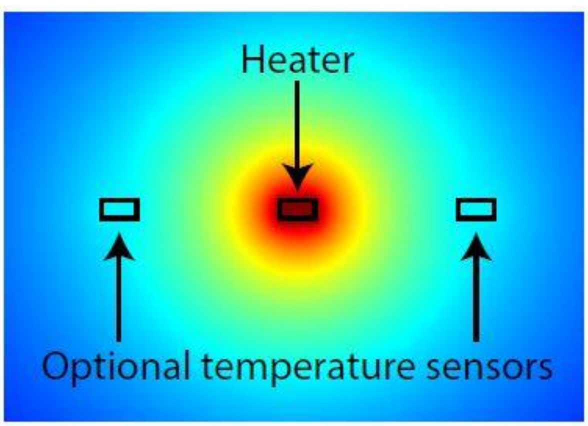

(a)

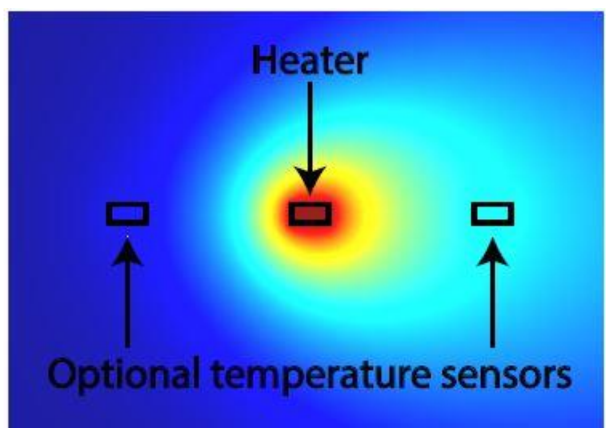

(b)

Figure 6: Schematic of thermal flow sensor (a)Temperature distribution without flow; (b)Temperature distribution with flow [22]

An upstream sensor can be used to increase the sensitivity and bidirectional sensing. Due to fluid flow, the heat is carried away by the fluid via convection. The upstream element is heated by the fluid as shown in Figure 6(b). A higher flow will result in more heat transferred, in turn, the temperature of the temperature sensor will be higher. Thus, the temperature of the sensor is measure of the flow.

The heat carried away by the fluid disturbs the temperature distribution around the heater. The typical temperature distribution is shown in Figure 7 [23]. When there is no flow or U=0, the temperature is uniformly distributed around the heater (case a). In presence of a flow, there is an asymmetry in the temperature profile (case b and c). Clearly, there would be a temperature difference between the two sensing elements in presence of flow. This temperature difference is taken as the output of the sensor and used to generate flow information. Unlike the hot-wire anemometer, the direction of the flow can be determined in these sensors. The sign of the output signal changes when the direction of the flow reverses. The important point to be noted is that the heat transfer to a fluid depends on specific heat capacity that varies between different fluids. So, a fluid to be measured needed to be characterized for the correct transduction of velocity to an electrical signal.

The benefit of using two elements is to eliminate common disturbances like temperature drifts by generating a differential signal. It can also be used to measure the temperature difference between two points in fluid flow when one of the points is heated.

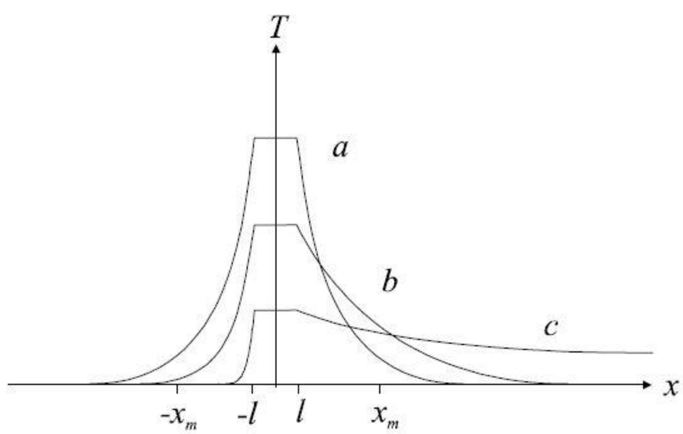

Figure 7: Temperature distribution as a function of position x in a channel. The heater is placed at x =- l and extends till x = l. x_m denotes the position of the temperature sensors. a: U=0; b: U is small enough to let the heat diffuse upstream [23]

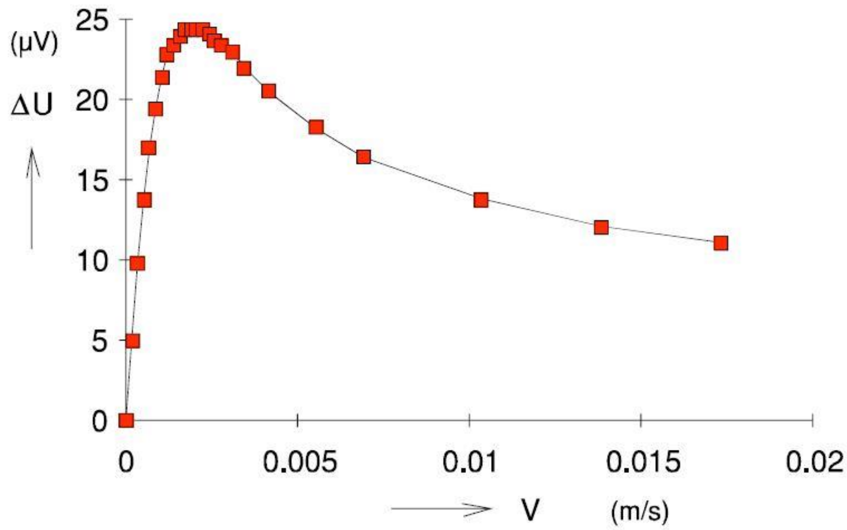

Figure 8: Flow characteristics of calorimetric sensor [24]

A typical calorimetric flow sensor output shows linear dependency on flow at small flow followed by maximum and a drop afterwards. Figure 8 [24] shows the same. Authors in [20] obtained such characteristics using water as fluid. The dimensions of the flow channel used were 1000 µm × 500 µm and the distance between the heater and the sensing elements was 1mm.

A calorimetric flow sensor is generally operated in two modes constant power or constant temperature. In constant power mode, the delivered by the heater is kept constant and temperature difference between the elements or sensors can be measured as a function of flow velocity [25]. For low-velocity increases linearly but at higher, the heater also starts to cool down, resulting in a peak determined by the flow sensor geometry and the fluid's thermal diffusivity [26]. The drawback of this mode is no limitation on the heater's temperature, resulting in burned heaters in a low convection situation. In constant temperature mode, the heater's temperature is kept constant, and the temperature difference between the sensors is a measure for the mass flow. Though this mode can prevent the burning of the heater but may result in high power dissipation at high flow rates. It also requires more complex electronics but has a higher flow range. Both modes depend on the thermal properties of the fluid and require adjustments according to it.

2.1.3 Time of Flight sensors

In time-of-flight sensor consists of a heating element and downstram temperatrure sensor. A heat pulse is generated by heater which is transferred to the downstream temperature sensor via convection. The pulse is affected by the flow velocity which attenuates the pulse and heat diffused from the pulse which broadens the pulse. The time between generation and detection by downstream sensor depends on the thermal conductivity and diffusivity of the fluid, heater-sensor distance ratio, and average flow velocity.

The thermal distribution of pulse as a function of time and distance is given by [27] assuming heater as a line source.

$$T(x,t) = \frac{q_0}{4\pi k t} e^{\frac{-(x-vt)^2}{4at}} \qquad 2.4$$

Where T denotes temperature distribution at time t,

x = distance from the heater,

t = time,

q_0 = pulse signal input strength,

k = thermal conductivity of fluid,

v = average flow velocity and,

α = thermal diffusivity

At high velocity, the peak of the thermal pulse is also travelling at a speed v, meaning that it can be a measure of fluid velocity. Thus, the flow velocity can be calculated by :

$$v = \frac{x}{t_{peak}} \qquad 2.5$$

At low velocity, the thermal diffusivity ($\alpha = {}^{k}/_{\rho c_p}$) has more influence on time of flight.

$$t_{peak} = \frac{-2\alpha + \sqrt{4\alpha^2 + v^2x^2}}{v^2} \tag{2.6}$$

For velocity lower than $v = D_t/d_{hs}$ signal tends to be too broad to be useful.

2.1.4 Why not thermal sensors?

Thermal flow sensors are most popular in the flow sensing industry because of their high accuracy and reliability at a low cost [16]. The introduction of MEMS technology has boosted the development of low-cost, small, and scalable thermal flow sensors with high sensitivity. They are currently primarily employed in automotive, aviation, bio-medical, and many other industries due to their robustness, fast response, and high sensitivity.

Still, thermal flow sensors are unable to deliver accurate measurements for low flow velocities. Despite considerable development in hot-wire sensors, they still suffer from heat loss due to conduction and poor accuracy at low flow velocities. Generally, calorimetric flow sensors show high sensitivity at low velocities as shown in **Error! Reference source not found.**, but saturate at higher velocities, limiting the dynamic range [17]. This problem can be eliminated by using combination of calorimeter and anemometer.

One can find many designs of hot-wire or hot-film and calorimetric sensors in the literature that claim to detect low airflow range. A few, who measured velocity lower than 1m/s have been listed in Table 2 [16]. However, the reasons for not selecting thermal sensors are the following:

- One of the prime reasons is thermal sensors are related to high temperature, the temperature of a hot wire can be in the range of (100˚C – 300˚C) which enough to change the temperature near the leaf.
- The leaf could also act as a heat sink which will be detrimental to the accuracy of the thermal flow sensor.

- The ones which can measure velocity less than 1m/s such as [28] and [29]are based complex fabrication process which may be difficult to replicate in a lab or cleanroom.

Table 2:Thermal sensors with detection range and sensitivity

Sensing element material	Configuration	Fluid Type	Detection Range	Ref
3C-SiC thin film heater	Hot Film	Air	0-9m/s	[30]
Polycrystalline silicon resistor	Hot Film	Air	0-30m/s	[31]
Pt Thermal element	Hot wire	Air	0-20m/s	[32]
Al/Si bond wire	Hot wire	Air	0.01–17.5 m/s	[33]
Al/polysilicon thermocouples Polysilicon heater	Hot Film	Gas,N_2	0–0.4 m/s	[29]
Pt heater and detector	Calorimetric	Air	0-10 m/s	[34]
Ni Resistors	Calorimetric	Air	0-1.4 m/s	[28]

2.2 Skin friction sensor

The relative motion between the fluid and surface causes the surface to experience a resultant force due to interaction. This relative motion or interaction can be well described in terms of stresses experienced by the surface. The shear stress acts tangential to the surface in the direction of the flow. Normal stress or pressure that acts normal to the surface. Measuring these stresses can give valuable insights into viscous drag, transition to turbulence, flow separation, and other flow phenomena. For low air flows of low to moderate shear stress is typically between 0.1 and 10 Pa [35].

The origin of the shear stress in a two-dimensional (2-D) interface layer can be schematically illustrated by Figure 9 [35]. The magnitude of the wall shear stress is proportional to the flow gradient.

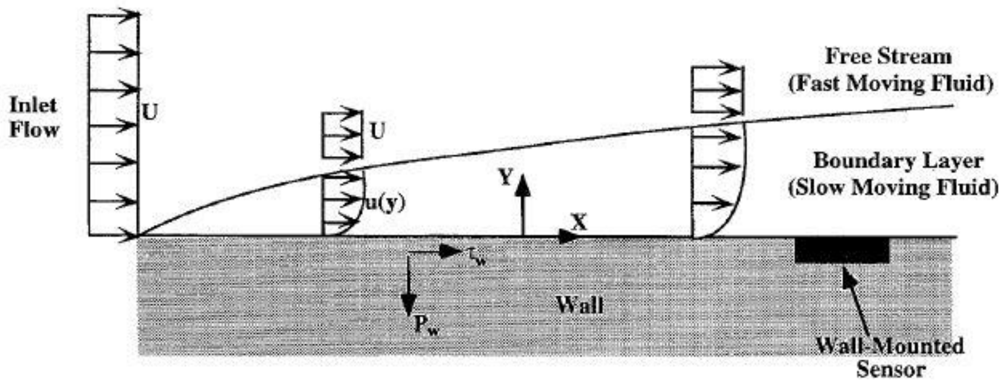

Figure 9: Schematic illustrating concept of Boundary layer, shear and normal stress associated to it [35].

$$\tau_w = \mu \left(\frac{\partial U}{\partial y}\right)_{y=0} \qquad 2.7$$

where μ is the dynamic viscosity of fluid and U is the streamwise velocity. Also, shear stress can be written for turbulent flow τ_w, as the sum of mean shear and fluctuating shear $\tau_w{}'$. The mean shear can be used to determine average properties like drag on surfaces. The fluctuating component is a representation of momentum transfer due to unsteady flow.

At low flows, the shear stresses can be *O(nN)* and corresponding displacements *O(Å).* Micromachined skin friction sensors can be of two types:

- Thermal skin friction
- Floating element type

For the thermal skin friction sensor, the skin friction in the fully developed boundary layer is proportional to the heat flux to the third power. Moreover, it is very difficult to reach high spatial resolution with thermal skin friction sensors [36] whereas with floating element type it is possible to attain high spatial resolution.

Authors of [35] were able to capture such low shear stress with a sensing scheme based on floating element shutter and integrated photodiodes as shown in Figure 10.

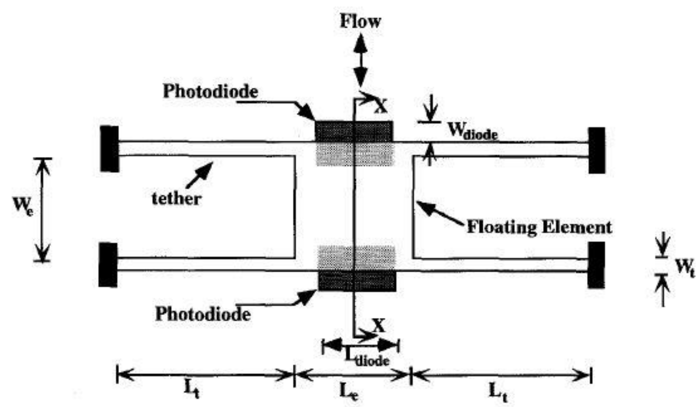

(a)

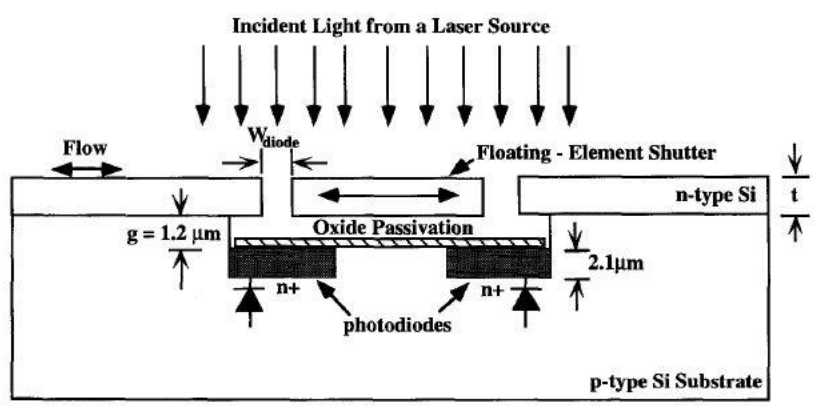

(b)

Figure 10: Schematic views illustrating the sensing principle [35] (a) Top view; (b) Side view

The sensor is made up of a floating element attached with 4 tethers (springs) as shown in the top view Figure 10(a). Photodiodes located under the leading and trailing edge of the floating structure are uniformly illuminated by the laser source situated above the

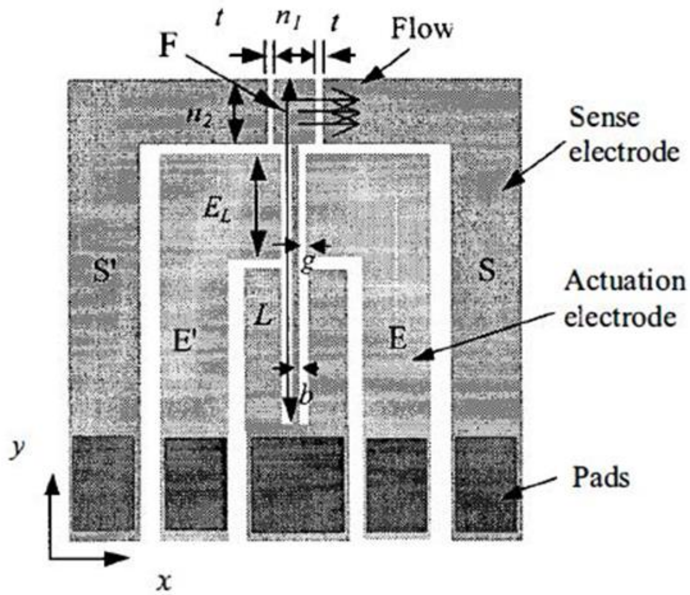

Figure 11: Schematic top view of the sensor [36]

floating structure, as shown in side view Figure 10(b). In the absence of any fluid, an equal area of both photodiodes is illuminated. This means that the photocurrent is equal in both diodes and the differential photocurrent is zero. When a fluid is made to flow, the floating structure slides (depending on the direction of flow) covering more area over one photodiode and exposing the other. Hence, there differential current 0 and is proportional to the magnitude and sign of wall shear stress.

$$\Delta I \propto \tau_w \tag{2.8}$$

Two designs for the floating element are used 1) 500×500×7 µm, 2) 120 ×120×7 µm. The former is more sensitive due to more mass of the floating element. It was able to measure shear stress of 0.01 Pa and lower in a laminar boundary layer.

A similar floating element technique with capacitive sensing was used by [37] to measure 0.1 to 2 Pa, with a spatial resolution of O(100 µm). The sensor was micromachined in an ultra-thin silicon wafer using wafer bonding and DRIE techniques. The floating element used is a cantilever-beam-like structure as shown in Figure 11.

The cantilever beam is designed to be stiff in the out-of-plane direction and soft for in-plane motion. The width of the wafer 50 µm whereas the width of the cantilever beam or floating element is 10 µm. Two sensing electrodes S and S' positioned on each side of the floating element, with a gap of 5 µm. Two actuation electrodes E and E' are positioned to test the floating element with small electrostatic force in the absence of fluid flow. The gap between the floating element and the actuation electrode is 25 µm. The spring constant of 80 is achieved with a beam length of 3 mm. According to the Authors, "the floating element would experience 10 to 50 nN of shear force 0.1 to 0.5 Pa shear stress range".

This sensor's advantage is that it is a MEMS sensor that can be worked with direct (using LCR meter) or differential capacitance techniques. The deflection sensitivity of the cantilever beam is 1 µm/Pa. The output sensitivity was found to be 20 fF/Pa and 0.5 V/Pa for direct and differential capacitance measurement. On the other hand, the drawback of this sensor is, it is not tested with fluid.

2.2.1 Why not a skin friction sensor?

The reason for not using skin friction sensors are following:

- One of the prime reasons is the size of these sensors is quite large i.e. 500 ×500 µm [35]. If place parallel to the leaf the size would be large enough to obstruct the flow and disturb the flow near the leaf
- The sensitive sensors such as [35], requires optical instruments to perform the measurements.
- Though, the floating element type can provide high resolution and sensitivity. The minimum shear stress of 0.01 Pa (Padmanabhan et al.[35]) and 0.05 Pa (Jiang et al. [37]) but according to [38] " these devices are fairly immature and require further development to become reliable measurement tool possessing quantifiable uncertainties".

A table has not been provided unlike thermal sensors because it is difficult to compare sensitivity of different sensors, as sensitivity is defined differently for different skin friction sensors. Using the information in this section, one can think of calculating drag force based on a floating beam or cantilever type of sensors instead of skin friction. In a next section, drag force sensors would be investigated.

2.3 Drag force sensors

Drag is a mechanical force that is generated by the interaction between a solid body and a fluid. Drag is generated by the relative motion between the body and the fluid regardless of object moves through a static fluid or whether the fluid moves past a static solid object. One of the sources of drag is skin friction between the solid and the molecules of the fluid. The skin friction depends on the properties of both solid and fluid for example; a smooth, waxed solid surface will produce less viscous force than a rough surface. In the case of fluid, “magnitude of drag force depends on the viscosity and relative magnitude of the viscous force to the motion expressed as Reynolds number” [39]. The significance of Reynold’s number is illustrated in Figure 12 [23].

Generally, drag force-based flow sensors contain one or more deformable shapes like cantilever or hair-like structures. When placed in a flow, these shapes experience a drag force. As a result, get deformed or tilted, as illustrated in Figure 13 [22]. The deformation or tilt can be measured using popular measuring techniques like piezoresistive, capacitive, and optical. The deformation can also be read out by resonance frequency, as with the tilt, the stiffness of the beam also increases [22]. For turbulent flows, the beams can start vibrating themselves. Beam actuation is required for laminar flows to measure the resonance frequency.

Drag force sensors can be divided into two regimes [40] :

- The first regime is stokes flow when the Reynolds number is less than 1 ($R_e \ll 1$). In this regime, the drag force is linearly dependent on flow. For a small spherical object, the drag force is given by

$$F_d = 6\pi\mu R v \qquad 2.9$$

Where μ is fluid’s dynamic viscosity, *R* is the radius of the sphere and v is the velocity of the flow.

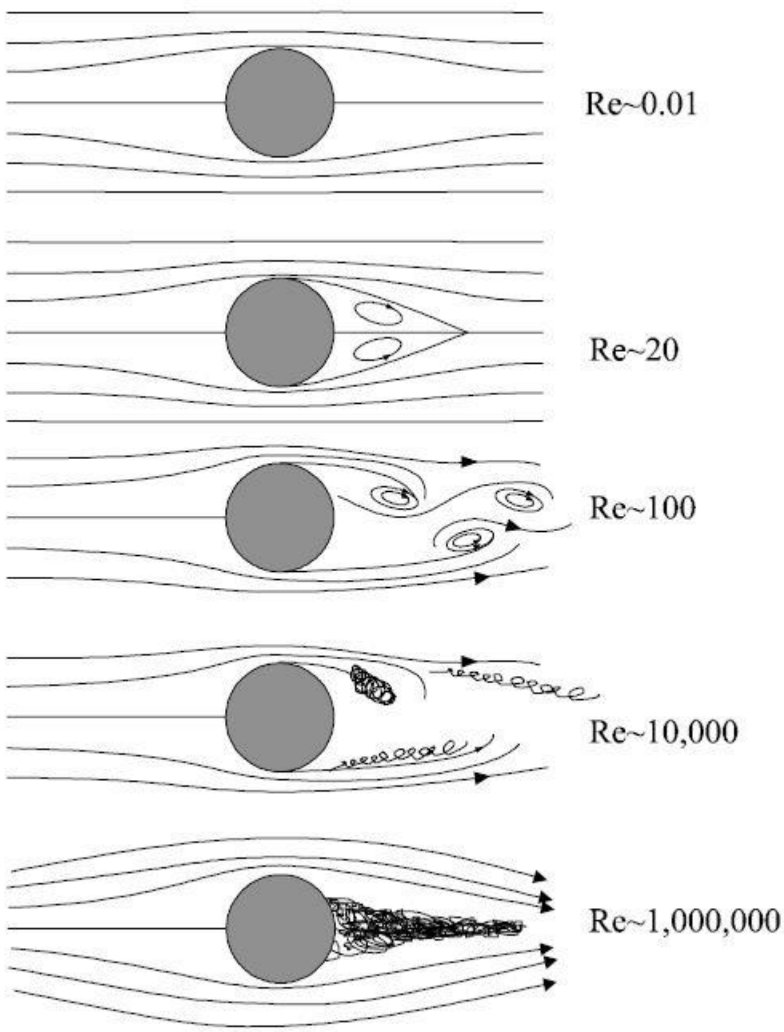

Figure 12: Flow behavior at different Reynolds number range past the infinite long cylinder [23].

- In the second regime, the flow velocity, and Reynolds number ($R_e > 1000$) is relatively high and the drag force varies quadratically to the flow velocity.

$$F_d = \frac{1}{2}\rho v^2 A C_d \tag{2.10}$$

where ρ is the density of the fluid, A is the cross-sectional area of the beam or solid in the flow and, C_d is the drag coefficient which depends on the fluid, flow properties, and the shape or geometry of the object.

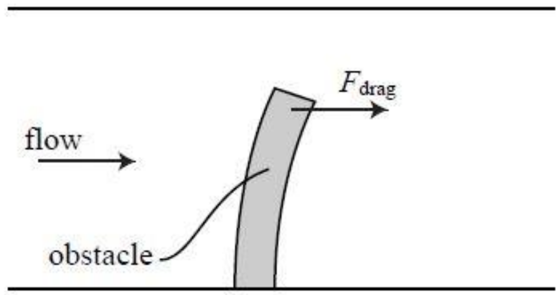

Figure 13: Scheatic view of drag force on hair like structure [22].

The drag coefficient is defined as the ratio of force per unit cross-section to kinetic energy per volume far away from the cylinder. Molding equation *2.10* gives:

$$C_d = \frac{F_d}{\frac{1}{2}\rho v^2 A} \qquad 2.11$$

C_d is not a constant but varies as a function of flow speed, flow direction, object size, fluid density, and fluid viscosity. It is essential to predict the drag coefficient accurately. The drag coefficient has complex dependencies not only on the object shape but also on air viscosity and compressibility. The compressibility factor can be neglected at low flows [41]. To account for viscous effects, the Reynolds number needed to be matched to accurately model the physics and predict the right drag. Hence, at low flows, the drag coefficient is a function of Reynold's number. At large flows, when compressibility of the fluid cannot be neglected, the drag coefficient is the function of Mach number (ratio of fluid's velocity past a boundary to the local speed of sound [42]). Figure 14 [36] shows the variation in the drag coefficient with the Reynolds number. Generally, the beam or cantilever is placed perpendicular to the flow

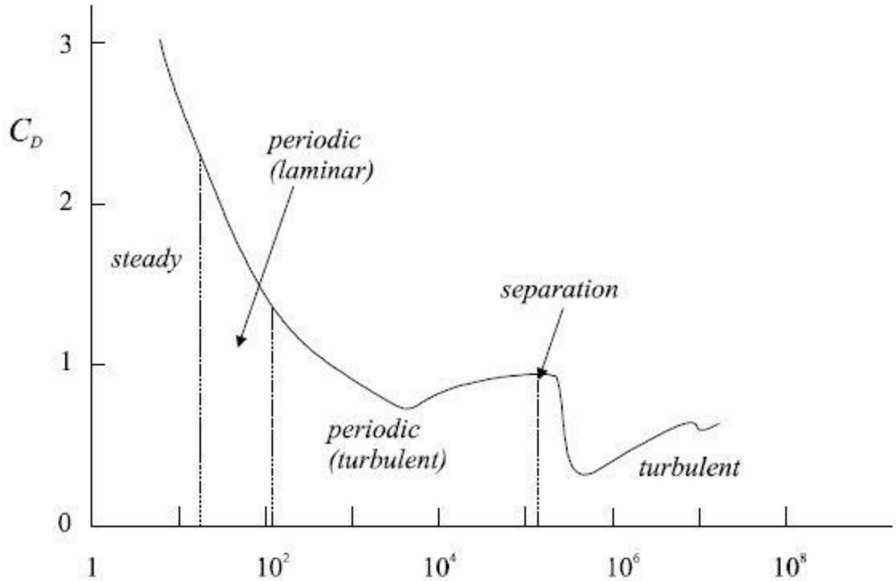

Figure 14 :Coefficient of drag as a function of Reynolds number[23]

2.3.1 Hair flow sensors

Hair flow sensors are designed to mimic living organisms such as arthropods, crickets, and fish who are equipped with highly sensitive flow sensors to help them survive in challenging environments.

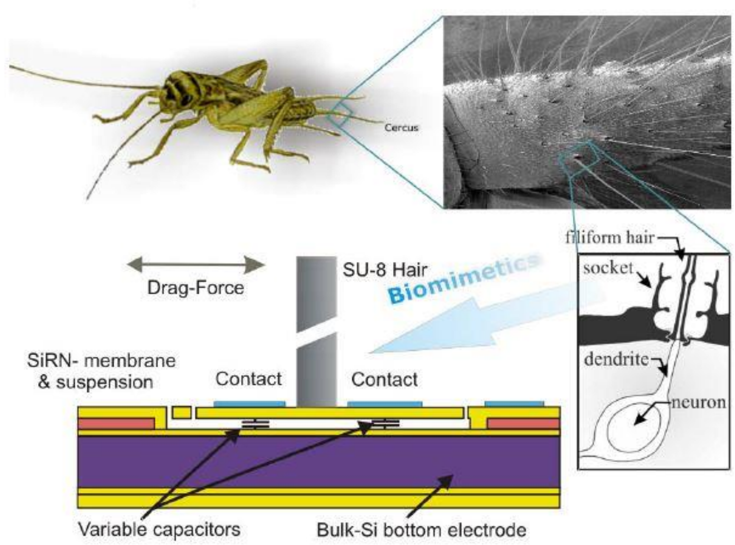

Figure 15: Hair flow sensor mimicking hair on cerci of cricket [42]

Inspiration to produce hair flow sensors is to achieve very high sensitivity and performance. Figure 15 [43] shows the hair flow sensor inspired by crickets. There has been a lot of progress in the development of artificial hair flow sensors since the first design came from MedX lab [44] in 2002 for underwater sensing based on lateral line of fish. Later, many notable designs came which claim better sensitivity and performance. One such design which came even before MedX was from the University of Japan by Ozaki [42] based on wind receptor hair of insect.

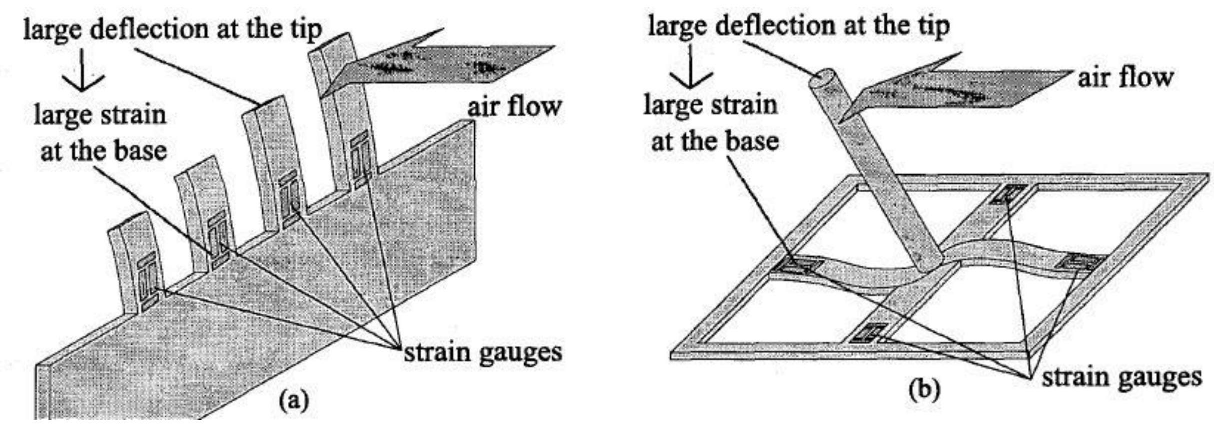

Figure 16 : Schematic diagram of Ozaki (a)1DOF and (b) 2DOF sensors [44]

The designs claimed to detect low flow velocity O(0.1)m/s – 2 m/s. There were two mechanical designs, one for 1DOF and the other for 2DOF, as shown in Figure 16 [45]. 1DOF model, composed of cantilevers and strain gauges, designed to detect the force component acting directly front or back of the cantilever whereas the 2DOF model had a long thin wire was attached to the center of a cross-shaped beam with the strain gauges fabricated at the end of the beams. The resistance of the strain gauges varies depending on the deformation of the cantilever against the flow. The velocity information can be extracted from the change in resistance of strain gauges. University of Twente team has been a significant player in developing hair flow sensors inspired by cricket using capacitive readout techniques. Many groups have been working on it since the early 2000s. The first generation of artificial hairs based on silicon-rich nitride demonstrated by [46] using narrow trenches in silicon. Later in 2005, the hair fabrication process was improved by [47], using SU-8 as a base material. The schematic view can be seen in

Figure 17. The SU-8 hair is aligned on the silicon-rich nitride membrane, acting as the upper plate for capacitive structure.

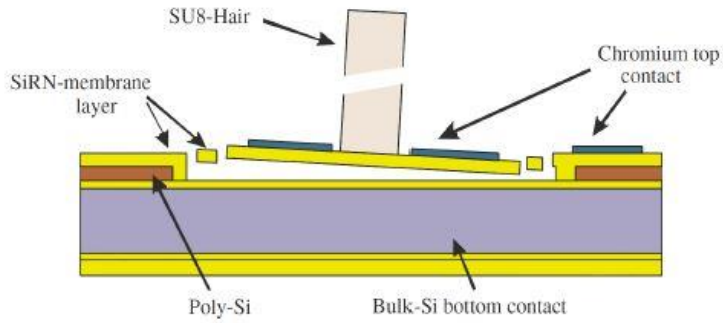

Figure 17: Schematic view of sensor structure with hair made up of SU-8 [46]

The silicon bulk act as bottom contact and the polysilicon membrane act as a sacrificial layer to achieve a rotatable membrane. The tilting of the hair in airflow is opposed by the torsional stiffness of the membrane. The deflection or tilting results in a change in the capacitance of the sensor. The length of the hair was increased by multiple layers of SU-8 stacked over each other, above 1mm [48]. Further advancements were made in hair length, inter-electrode gap, the membrane shape, and torsion beam geometry by [49] which result in 100 times increase in sensitivity measuring 1mm/s of flow amplitude.

The capacitive sensor can be modelled as a 3 tier system consisting of the mechanical system of the torsional hair, the aerodynamic system, and the capacitive transducer system [50]. The performance of the system can be evaluated FOM (figure of merit), which is defined as the product of bandwidth and sensitivity. To obtain a high FOM, long thin hair made of low density with a low stiffness of torsion spring is required.

2.3.2 Cantilever based flow sensors

Wang et al. [51] came up with a micro-scale airflow sensor based on a free-standing cantilever structure by depositing a platinum layer on silicon nitride to form a piezo resistor and etching the resulting structure to create a free-standing micro-cantilever as shown in Figure 18. The cantilever deflects or deforms in downward direction when the flow is passed over it. The deformation resulted in variation in the resistance of the piezoelectric layer. The airflow velocity could be directly measured by measuring the change in resistance using an external LCR meter. The authors claimed to achieve high sensitivity of 0.0284 Ω/ms^{-1} , velocity measurement limit of 45 m/s and, a response time of 0.53 s.

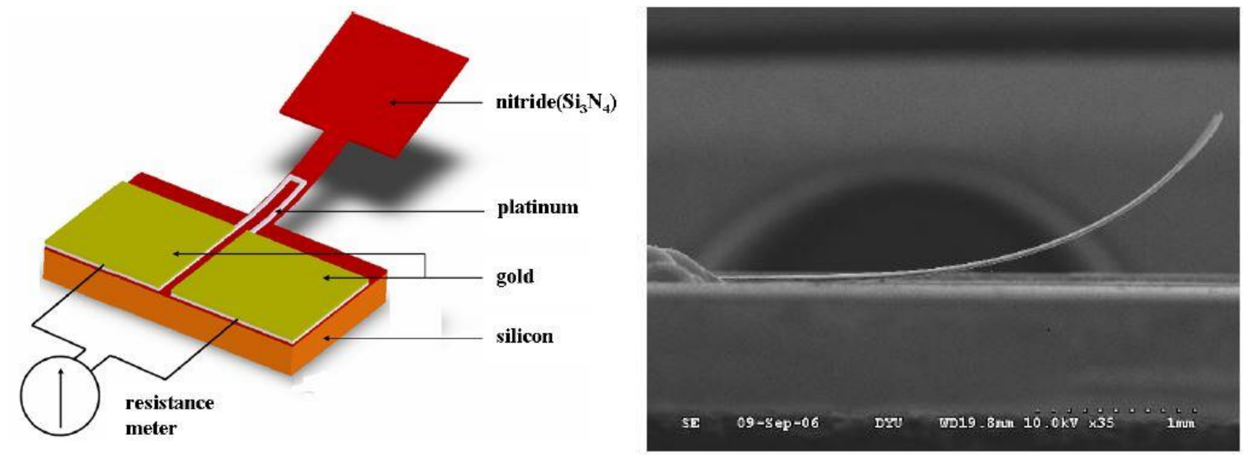

Figure 18: (Left)schematic view of the gas flow sensor; (right) side view SEM image of the cantilever [50]

To investigate the relation between the sensitivity and physical dimension of the cantilever they fabricated 3 different cantilevers with a beamwidth of 400 μm,1200 μm and, 2000 μm and found out that sensitivity increases as the width of the cantilever beam is increased.

Similar sensor presented by Du et al. [52] and team, calling it a drag force sensor. The sensor was made up of a thin silicon plate and two short cantilevers. The cantilevers connect the plate to the silicon substrate as shown in Figure 19(a) and (b). In an airflow, the silicon plate will experience a drag force, bending the two silicon cantilevers attached to the plate. The velocity information is extracted by measuring the strain in the cantilevers. The drag force sensor was simulated with ANSYS software, analyzed with fluid mechanics principle, and fabricated using MEMS-based technology.

The strain of the cantilever is simulated at room temperature under the flow speed from 0.4 m/s to 21 m/s. and compared with the theoretical strain, found to be almost equally as shown in Figure 19 (c). The sensor design almost matches with the sensor design found in one of the early papers by Y Su et al. [53] except the length of the cantilever beams which was comparatively larger in Y Su design and tilted at an angle of $20°$ from the silicon plate as shown in Figure 20 (a). The strain gauges were integrated at the bottom

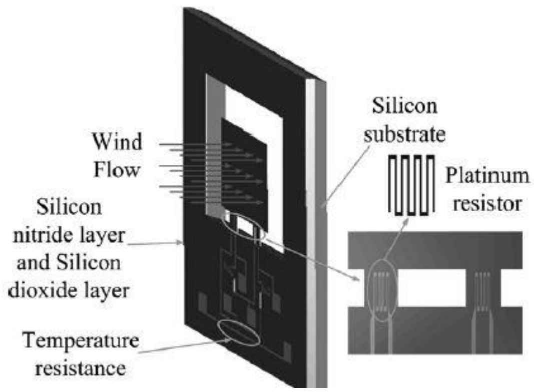

(a)

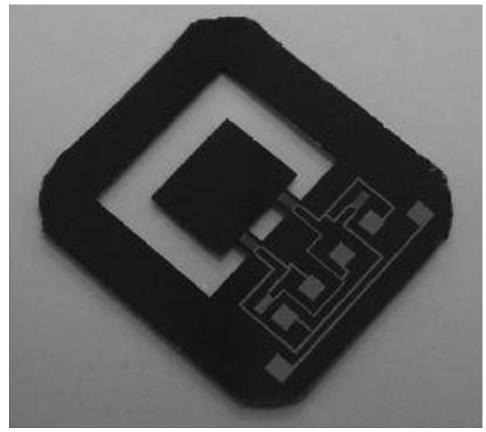

(b)

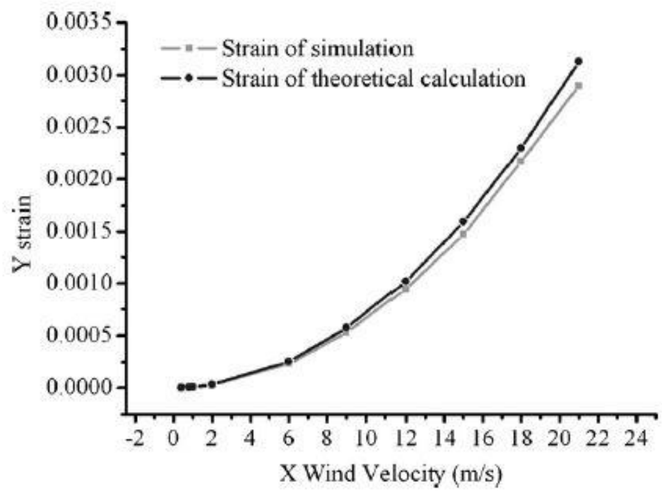

(c)

Figure 19: (a) Schematic view of full sensor;(b) Image of final sensor; (c) curve comparing Simulated and theoretical strain [51]

of the cantilever at the substrate side. The structure was used to measure the velocity profile in a steel pipe of inner diameter 7 mm, claiming the experimental minimum detectable velocity to be 7 cm/s. A set of cantilever beams were fabricated as shown in Figure 20 (b). The length of the cantilever and the area of the plate was varied ($100 \times 100\ \mu m^2$, $150 \times 150\ \mu m^2$, $200 \times 200\ \mu m^2$). The results indicated that the flow sensitivity $\left(\frac{\Delta R/R}{V^2}\right)$ is higher for longer cantilever whereas the deflection sensitivity $\left(\frac{\Delta R/R}{y(0)}\right)$ is higher for shorter cantilever beams. V is the velocity of fluid and y(0) is the displacement of the cantilever at the junction.

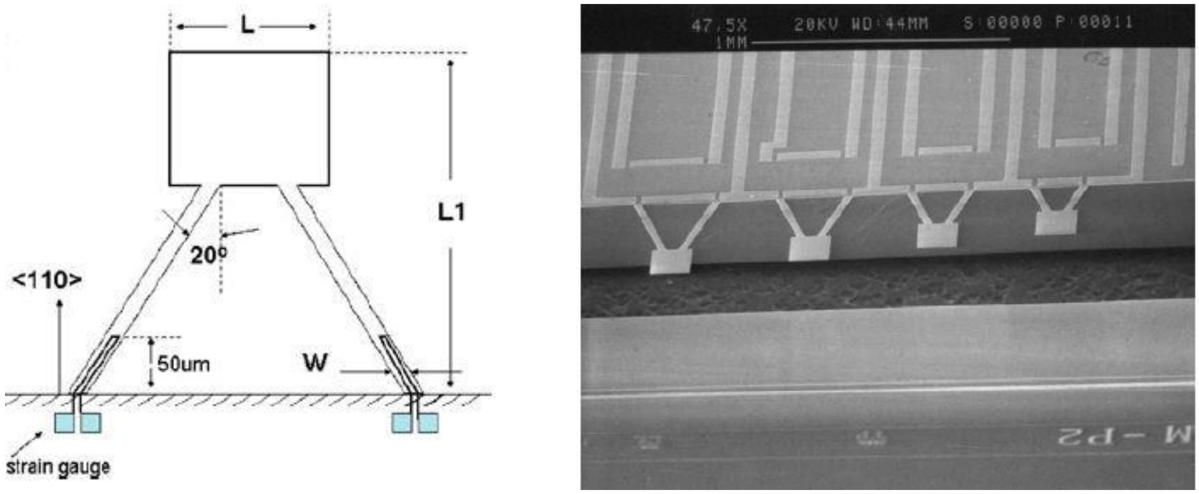

(a) (b)

Figure 20: (a) Schematic diagram of cantilever beams and integrated strain gauges;(b) Set of silicon cantilevers with different length and area of plate [52]

2.3.3 Why not drag force sensor?

Different types of drag force sensors are analyzed in previous sections and classified as hair flow sensors and cantilever-based sensors. Drag force sensors can be highly sensitive and detect velocity as low as 0.1m/s like thermal flow sensors, but the average drag force gives the flow information on the whole structure instead of a point. Without a doubt, hair flow sensors can design to achieve very high sensitivity and performance and detect a small flow as 1mm/s (by bio-inspired capacitive hair flow sensor [43]). But the fabrication process can be cumbersome and hard to replicate.

On the other hand, the cantilever-based drag force sensors can be fabricated with MEMS-based technology [46-47]. One of the drag force sensor's major advances is that they can be easily mounted on the probe, presenting a narrow vertical structure perpendicular to the leaf. The flow near the leaf is expected to be least affected by such an arrangement. Hence, using a cantilever-based drag force sensor that can be fabricated by existing MEMS-based technology is recommended for the application.

In the next chapter, such a sensor's design will be investigated based on the design presented in chapter 2.

Chapter 3: Design and Modelling

In Chapter 2, potential flow sensors that can be used for the measurement were discussed along with their advantages and drawbacks. Drag force-based flow sensors seemed to be the right candidate for measuring airflow near a leaf (refer to section 2.3.3) because they can be made highly sensitive even with the small size of sensing elements like bio-inspired hair flow sensors and cantilever-based sensors. Undoubtedly, bio-inspired hair flow sensors could be the most suitable sensor because of the high sensitivity and small size of hair-like structure but due to fabrication complexities and poor repeatability, it does not seem to be a wise choice. On the other hand, cantilever-based flow sensors have high sensitivity, and a small sensing element size (larger than bio-inspired flow sensor) and can be fabricated with available MEMS-based technology [46-47].

In this chapter, the design and modeling of a cantilever-based flow sensor will be discussed along with simulations of the sensor to optimize the sensitivity and the design. The theoretically calculated drag force on the cantilever is confirmed with simulations. All the simulations are performed in COMSOL Multiphysics 5.5.

3.1 Idea of Design

The design presented by Du et al. [52], made up of a square plate connected to the silicon substrate via two thick cantilevers (see Figure 19) can measure wind velocity in the range of 18- 21 m/s. This range is relatively high compared to airflow near a leaf. If the sensor can be scaled down to measure lower wind speed, the cantilevers should be thin and long to decrease the stiffness or increase sensitivity. As the cantilevers become thin and long, they would now be more prone to the sideways movement or movement perpendicular to the flow direction. This sideways movement could be reduced by employing the idea from the design of Y Su et al.[53]. In their design, the cantilevers were designed at an angle from the silicon plate, as shown in Figure 20 (a). With this design, they achieved high sensitivity in the flow direction (refer to section 2.3.2). They claimed to detect the minimum speed of 7cm/s but did not show the same in the plotted measurements results.

Both designs used integrated strain gauge at the junction of the cantilever and substrate as shown in Figure 19 and Figure 20, and the change in resistance gave the information about the flow velocity. These designs can be improved or made more sensitive if a capacitive readout technique can be used in such a design. In this thesis we propose a seesaw design with a capacitive readout technique, as shown in Figure 21, which can be fabricated on SOI (silicon on Insulator) wafer using MEMS-based technology in the lab at the University of Twente [54].

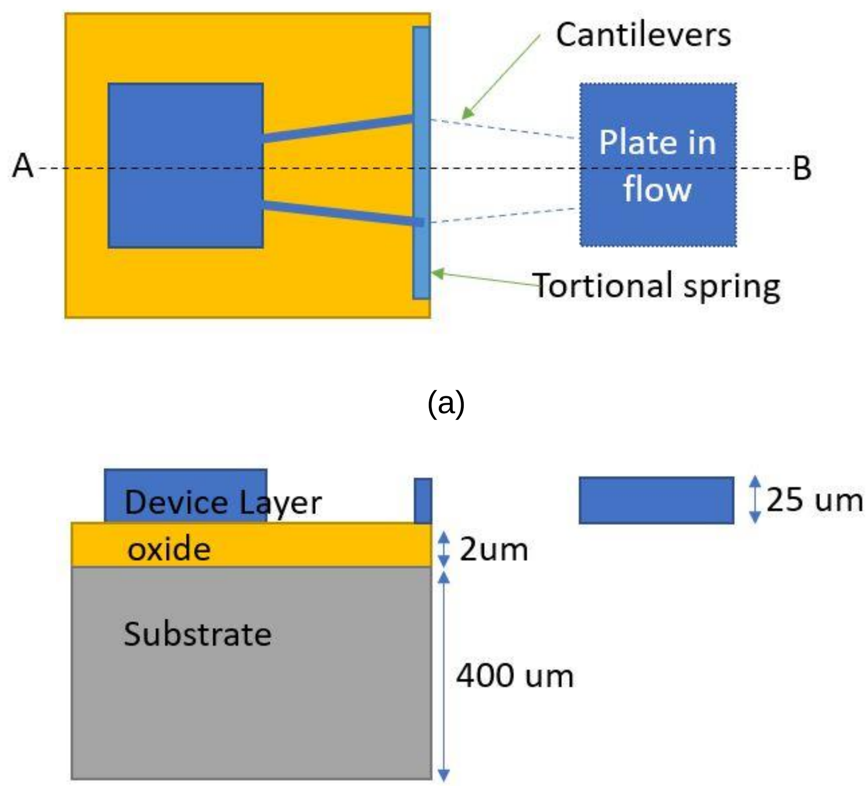

(a)

(b)

Figure 21: Schematic representation of the proposed airflow sensor on SOI wafer (a) Top view;(b) Side view along line the line AB

The design consists of two silicon plates on both ends, connected to a torsional spring in the middle using two cantilevers. The cantilevers are placed at a particular angle to the spring. One of the silicon plates will be free (the substrate will be removed from beneath) and placed in the airflow while the other will form a capacitance with the substrate as shown in Figure 21 (a). When the free plate is placed in a flow, the sensing principle is the drag force will deflect the plate, which will deflect the plate forming capacitance with the substrate. As the other plate moves, there will be a change in capacitance, giving information about the flow. The design aims to get a change in capacitance of more than 200 fF at a flow of 1m/s. The capacitance calculations are given in section 3.7.

3.2 Modeling and Calculations

The whole design has three components:

1. Plate
2. Torsional spring
3. Cantilevers

3.2.1 Plates

The plates or silicon plates experience drag force when placed in the flow. The drag force is proportional to the size or area of the plate [53]. The drag force can be calculated by the analytical formula given by equation 2.9. Considering the dimension of the plate to be 400 × 400 μm^2, velocity (v)= 1 m/s. To calculate C_d one should calculate the Reynold number first which is given by the following equation:

$$R_e = \frac{D\rho v}{\mu} \tag{3.1}$$

where μ is the dynamic viscosity of the fluid, ρ is density, v is the velocity of the fluid and D is the characteristic length. The values of these parameters for air at 15˚C are given in Table 3.

Table 3: physical parameters for air at 15 ℃

Parameters	Values
μ	1.802 × 10^{-5} $kg/m.s$
ρ	1.225 Kg/m^3
D	400 μm

The Reynolds number could be calculated as 27. Now, approximate the value of C_d is 2 from Figure 14. Inserting this in equation *2.10*, the drag force can be calculated as 196 nN (nano Newton).

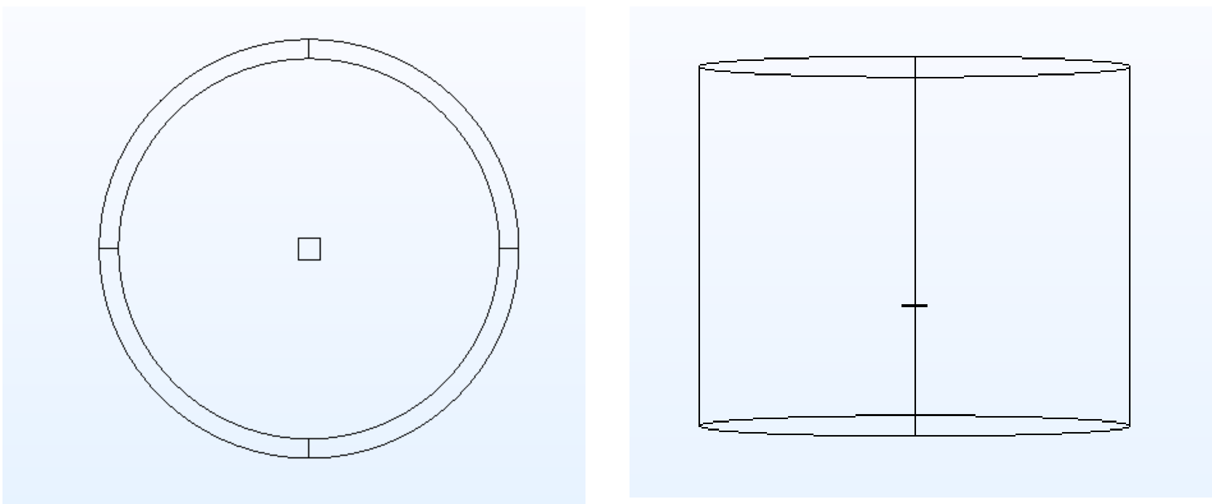

(a) (b)

Figure 22: The schematic view of the square plate inside a cylinder (a) X-Y plane view;(b)Y-Z plane view

The theoretical calculation is verified by building a simulation model in COMSOL Multiphysics 5.5. The 3D model is built in a submodule called Laminar Flow of Fluid Flow module. The model consists of a square plate (whose dimensions can be input in globally defined parameters) placed in airflow of 1m/s. The flow is represented by a cylinder as shown in Figure 22. There are several ways to calculate drag force in physics. One of the ways is to integrate the total stress. To do so, the surface integration operator is defined under the Derived values node. After applying the physics-controlled normal mesh, the model is simulated, and the results are illustrated in Figure 23. The Drag force can be calculated for $400 \times 400\ \mu m^2$ and velocity (ν)= 1 m/s as 192.28 nN.

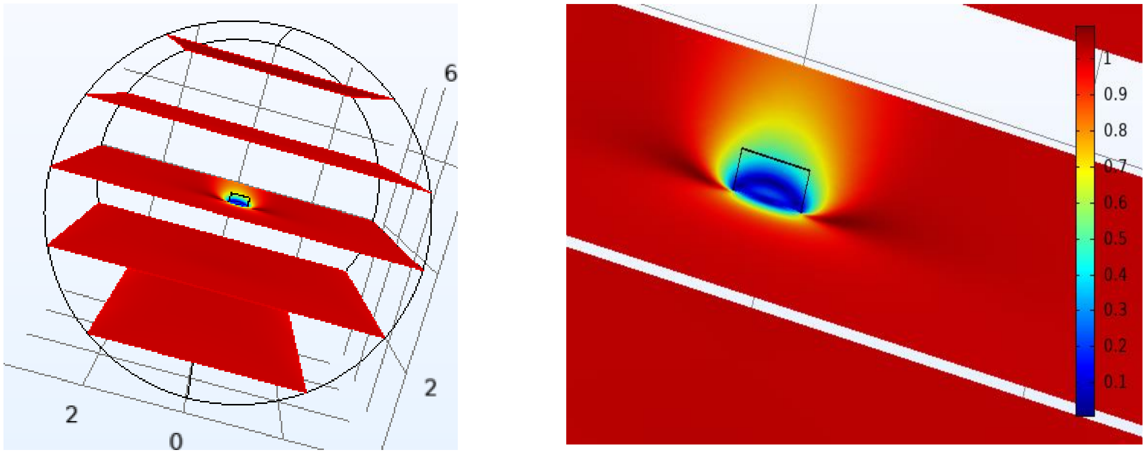

(a) (b)

Figure 23: Slice plot showing the fluid velocity variation near plate (a)Normal view;(b) Close-up view.

3.2.1.1 Convergence Study

The simulations are verified by the convergence study. In simple language, convergence study is related to how small the elements need to be to ensure that the results of finite element (FEA) analysis are not affected by mesh size. Thus, the model is subjected to different mesh sizes from Normal to Extremely fine. The variation in the drag is listed in Table 4.

Table 4: Mesh Convergence study

Mesh Size	Number of tetrahedral elements	Drag Force (N)
Normal	46059	1.9228E-7
Fine	123059	1.9293E-7
Finer	231636	2.0327E-7
Extra Fine	516599	2.0660E-7
Extremely Fine	1551294	2.0660E-7

The convergence study shows that drag force does not change when mesh size transitions from Extra fine to Extremely fine. Hence, the final value for the drag force is 206.6 nN, which is differs from the theoretically calculated drag force by 4.5 %. The idea of the mesh size can be related to the number of elements of tetrahedral and triangular elements. As the mesh density increases, the number of such elements increases. To get an idea, table 4 contains a column for the number of tetrahedral elements at different mesh sizes. Similarly, drag force is calculated for plates of various dimensions given by Table5. The drag force increases quadratically with plate size as shown in Figure 24. Simulated and theroretical value of drag force has been plotted in Figure 24. The error reduces for larger area.

Table 5: Drag force variation with area of plate.

Plate size (μm^2)	Simulated Drag Force (nN)	Theoretical
100×100	24.9	12.5
200×200	65.2	49
300×300	127.7	110.25
400×400	206.6	196
500×500	298.8	306.25

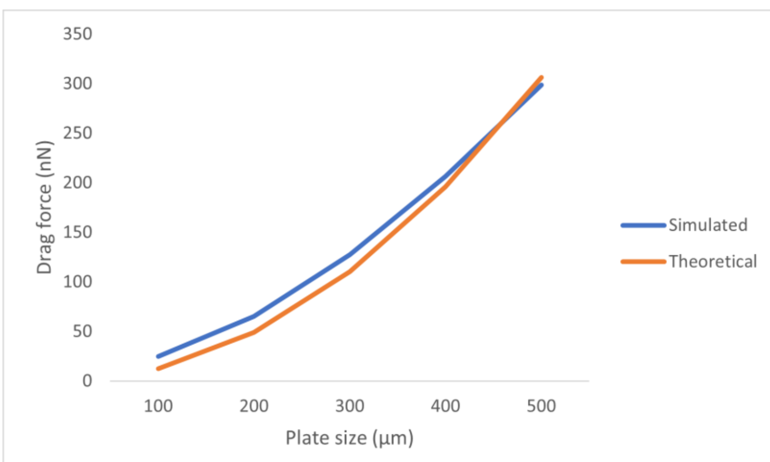

Figure 24: Drag force as a function of the size of the plate.

3.2.2 Torsional Spring

Torsion can be defined as the twisting of a structural member loaded by couples (torque) that produces rotation about the member's longitudinal axis. In simple words, the member is loaded so that the stress resultant is a couple about the longitudinal axis, and the response is a twisting motion of the axis [55]. Couples that produce twisting of a bar are called torques, twisting moments, or twisting couples.

When a circular bar is subjected to a twisting moment, each small section rotates about the longitudinal axis. The plane section remains the same and radii remain straight. At any point, the magnitude of shear stress is proportional to the distance from the center of the section. The direction is perpendicular to the radius connecting that point to the axis. The deformation and stresses are illustrated in Figure 25. When a circular bar is loaded in this manner, it is said to be in pure torsion or a state of pure shear. The angle of twist can be given by:

$$\theta = \frac{TL}{GJ} \qquad 3.2$$

Where:

θ= Angle of Twist (radians), *T*= Torque applied, *L*= length of the member, *G*= shear modulus, *J*=polar moment of inertia

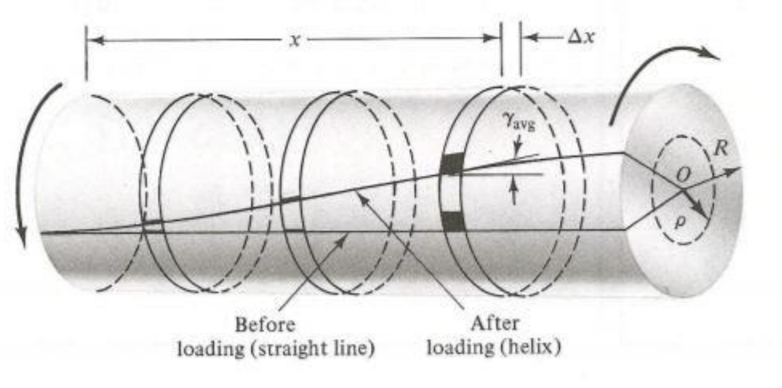

Figure 25: Schematic illustration of a circular beam in pure bending [53]

The above formula is not valid for non-circular structures. When a non-circular bar twists, each section is rotating about its torsional center. Sections do not remain in-plane but wrap, and the direction of radial stress is not necessarily normal to a radius. For non-circular shapes equation *3.2* can be written as:

$$\theta = \frac{TL}{KG} \qquad 3.3$$

where *K* is a factor dependent on form and the dimensions of cross-section [56]. For a circular cross-section, the *K* is equal to the polar moment of inertia. For cross-sections other than circular the *K* would be less than *J* or maybe a small fraction of *J*.

The value of K for a rectangular cross-section as shown in Figure 26 can be calculated from [56]:

$$K = ab^3 \left[\frac{16}{3} - 3.36 \frac{b}{a} \left(1 - \frac{b^4}{12a^4} \right) \right] \qquad 3.4$$

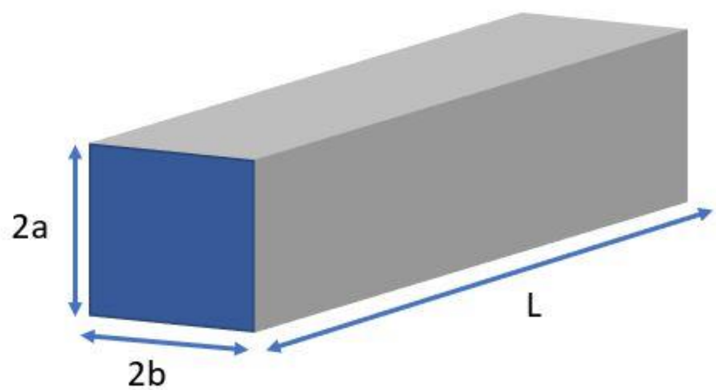

Figure 26: cross-section of rectangular torsional spring

Once the value of K is known, for small-angle θ, the equation can be written as :

$$T = K_t \theta \qquad 3.5$$

Where, K_t is the torsional spring constant given by:

$$K_t = \frac{KG}{L} \quad 3.6$$

Note that equation *3.4* is given in a simplified form involving an approximation, with a resulting error not greater than 4% [54]. Using equation *3.6* torsional spring can be calculated for a particular length. The spring stiffness is proportional to the factor, bulk modulus, and inversely proportional to the length. If the width of the cross-section is increased, from equation *3.4*, the value of K would increase and, in turn, spring constant would increase, which would decrease the sensitivity. To make the device more sensitive, the width should be kept low. In MEMS-based fabrication, at the University of Twente [54], the minimum feature size should be greater than 3.5 to reproduce accurately. Thus, the minimum width of the spring could be assumed as 4. The thickness torsional spring is fixed as 25 because of the width of the device layer in an SOI wafer. Thus, factor from equation *3.4*, for Figure 26, where 2a= 25 and 2b=4 can be calculated as:

$$K = 479.6 \times \ 10^{-24} m^4 \quad 3.7$$

Effectively there are two torsional springs at each end of the torsional beam with effective length (L_e) of 126 μm. A larger length of the spring would result in higher sensitivity at the cost of stability of the sensor. The structure would be more susceptible for movement in x-direction due to gravity.

3.2.3 Cantilevers

Cantilevers placement or the angle at which cantilevers are placed would help to reduce the sideways movement and would be seen in section 3.3.1.4. Figure 27 shows the simulated design in COMSOL Multiphysics 5.5. The cantilevers are placed at an angle (θ) to minimize the sideways movements. The dimensions of the cantilever are assumed to 1006 μm in length and 24 μm in width. The reason to assume this length is to make sure the sensing element is long enough to sense the flow with minimum hindrance to the flow and get the desired capacitance change.

3.3 Design Simulations

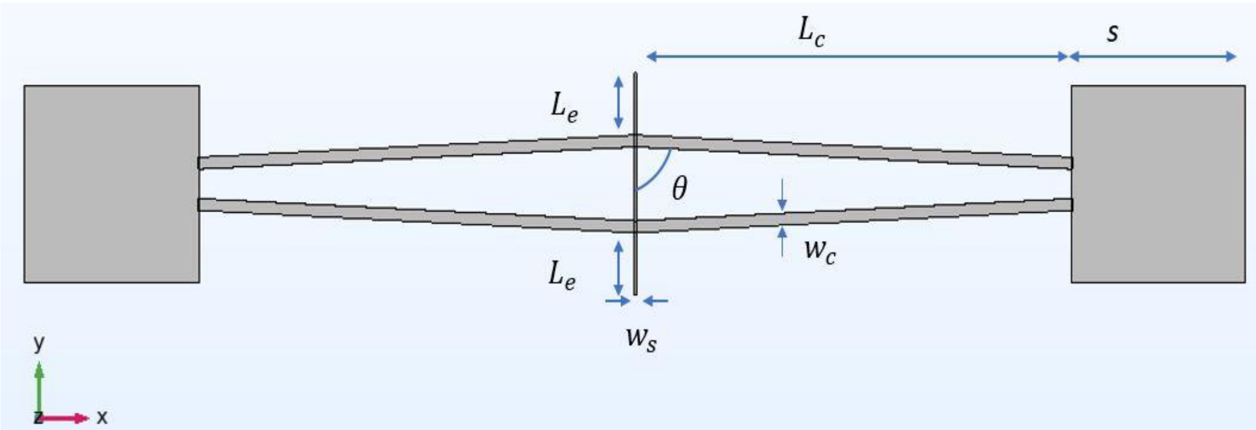

Figure 27: Screenshot of Simulated Design.

The design is simulated in COMSOL Multiphysics 5.5. The dimensions are illustrated in Figure 27. The dimensions are also listed in Table 5. All the dimensions are in micrometers.

Table 6: Dimensions of the initial design

Components	Dimensions (μm)
Side of plate (s)	400
Width of spring (w_s)	4
Total length of the spring beam (L_t)	450
Effective length of each spring (L_e)	126
Width of cantilever (w_c)	24
Angle of Cantilever to spring (θ)	87.44°
Length of cantilever (L_c)	1006

The model is built in structural mechanics module. After applying appropriate boundary conditions such as fixed constrain on both ends of the spring, boundary load of 206.6 nN on the plate in the z-direction, the model is simulated, and the displacement of the plate in the z-direction (d_z) is 0.632 as shown in Figure 28.

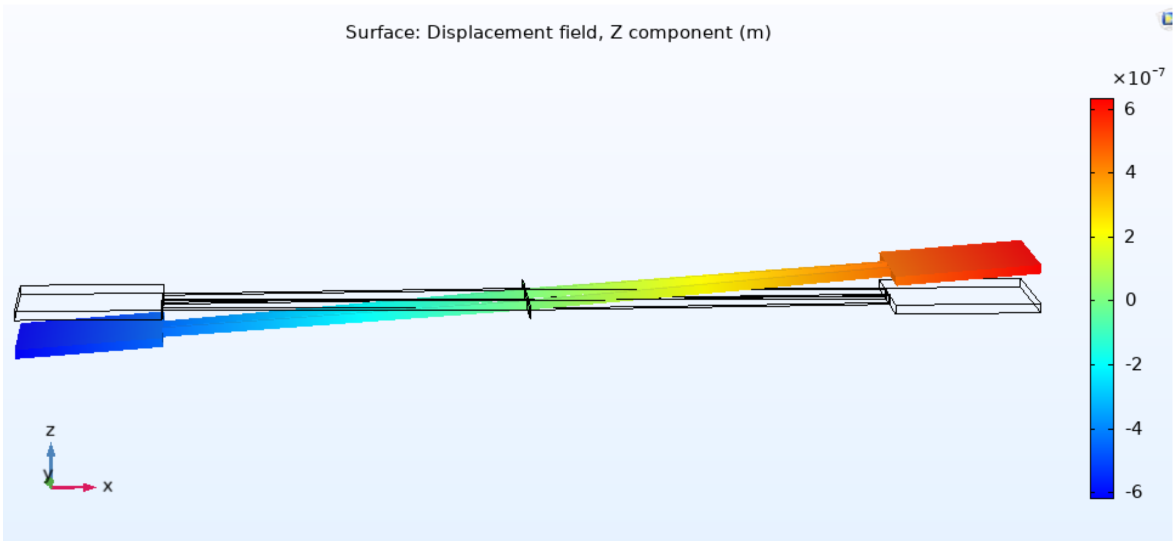

Figure 28: Screenshot showing displacement of plate on applying drag force.

As discussed in previous sections, the movement of the structure in another (lateral) direction is also very important to analyze. Figure 29 shows eigenfrequencies at which the structure would vibrate in different modes.The structure can vibrate in six modes, the dominant mode at lower frequencies is the mode for which device is designed (see Figure 29(a)). The next mode which shows the sideways movement of the structure occurs at nearly 4 times the frequency of first mode. The other modes occur at higher frequencies and do not concern the stability of the design with given dimensions Table 6.

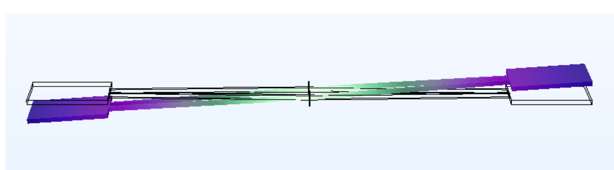

(a)Eigen frequency: 697.17 Hz

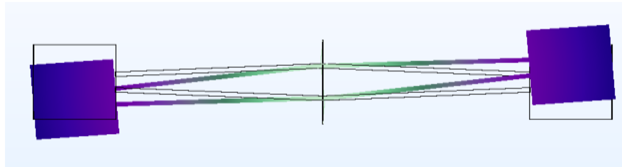

(b) Eigen frequency: 2496.2 Hz

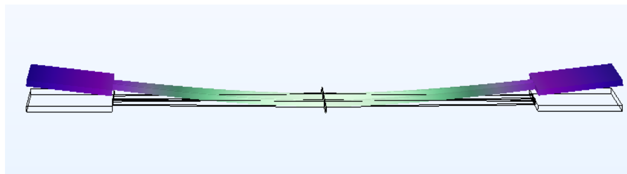

(c) Eigen frequency: 6821.2 Hz

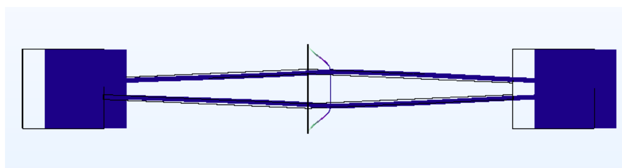

(d) Eigen frequency: 16621 Hz

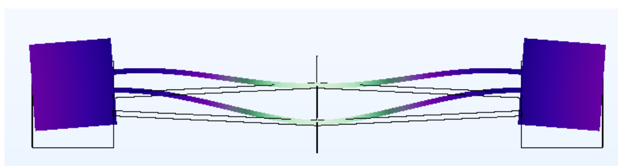

(e) Eigen frequency: 28127 Hz

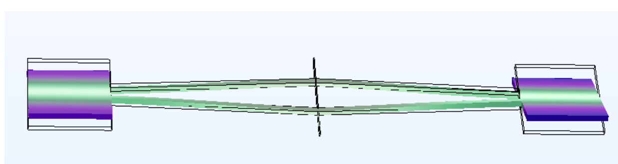

(f) Eigen frequency: 37944 Hz

Figure 29: Resonance modes of the structure.

3.3.1 Optimization

The design can be made more sensitive (increase in change in capacitance) either by increasing the size of the plate or by increasing the effective length of the spring. In this section, we will see the effect parameters given in Table 6 on the maximum deflection and mode frequencies. Such analysis would give help in understanding effect of individual parameter on the maximum defelction and sideways movement of the structure.

3.3.1.1 Plate optimization

Increasing the size of the plate (keeping the other parameters constant as given in Table 6, would surely increase the deflection of the plate deflection of nearly 1 μm could be achieved with a plate of area 500 $\times$ 500 μm^2, but it would also produce a lot more hindrance to the airflow than a plate of size 400 $\times$ 400 μm^2. On the other hand, decreasing the size of the plate will reduce the deflection of the edge of the plate to 0.338 μm, hence, also the sensitivity. Hence, it is recommended to keep the plate size to be 400 $\times$ 400 μm^2.

3.3.1.2 Spring length

The maximum deflection can be controlled by adjusting the effective length of the spring and sideways movement can be controlled by adjusting the angle and the thickness of the cantilever. Table 6 shows maximum deflection at different lengths of spring keeping the thickness cantilever and θ constant. Maximum deflection (d_z) increases linearly with effective length as shown in Figure 30.

Table 7: Maximum deflection at different spring length

Cantilever Thickness (μm), θ (degree)	Effective length (L_e)	Maximum Deflection (d_z)	Mode1	Mode2
24, 87.42	126	0.632	697.17	2497
24, 87.42	134	0.677	673.7	2340
24, 87.42	142	0.72	652.8	2202.5
24, 87.42	150	0.762	634.75	2082.8

whereas modal frequency decreases, which should be the case. As L_e increases, spring stiffness decreases, thus the mode frequencies.

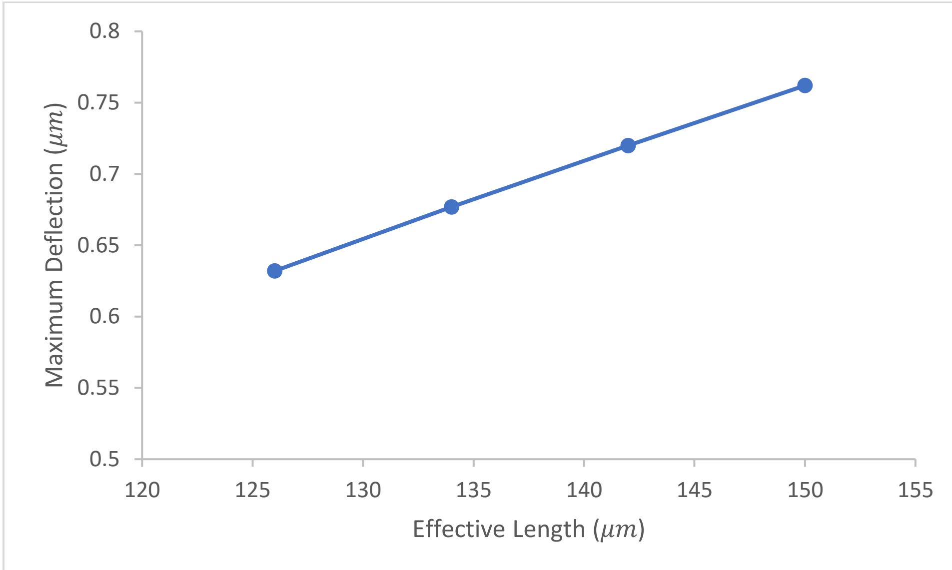

Figure 30: Maximum deflection variation with Effective length

3.3.1.3 Angle between cantilever and spring

Table 8 shows the variation in d_z and modal frequencies with θ at a constant thickness of cantilever beams. Maximum deflection (d_z) is dependent on effective length (L_e) of spring, which remains nearly unchanged with θ, mode 2 frequency corresponding to the sideways movement has increased as shown in Figure 31(left). In other words, the structure is more resistant to sideways movements. For an idea, 0.56° increases in θ increase the total length of the spring by 20 μm. As expected, mode 1 frequency nearly unchanged because of spring stiffness remains unchanged. Overall, increasing the θ makes the structure more resistant to the sideways movement without affecting the maximum defelection.

Table 8: Mode frequencies at different Angle between cantilever and spring θ

θ(degree)	$w_c(\mu m), L_e(\mu m)$	$(d_z)(\ \mu m)$	Mode1(*Hz*)	Mode2(*Hz*)
87.42	24,126	0.632	697.17	2497
86.85	24,126	0.6324	697.15	2643
86.29	24,126	0.6325	697.14	2788

85.71	24,126	0.6327	697.03	2935

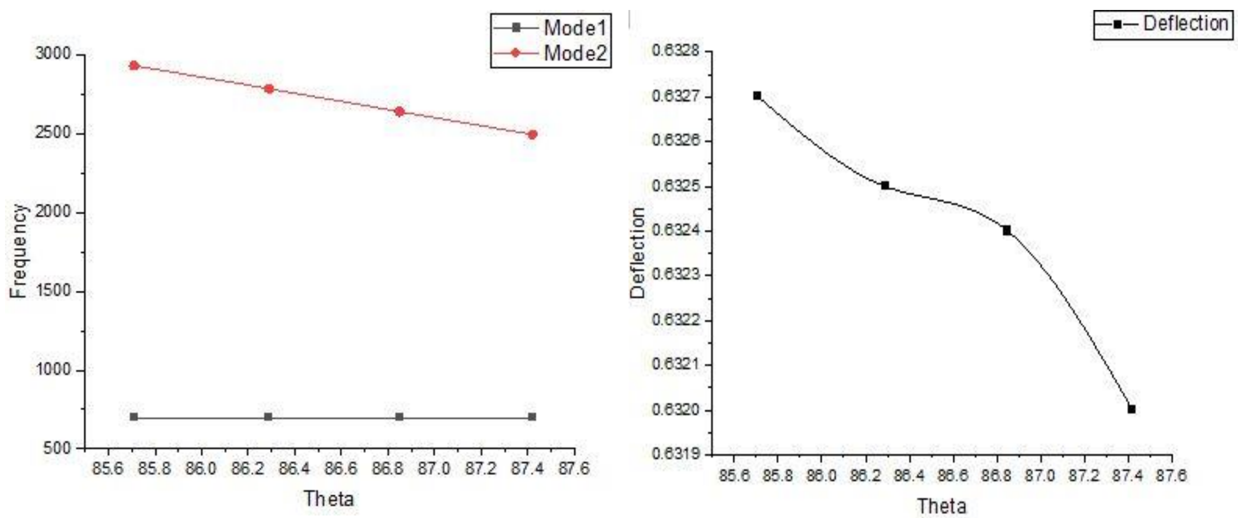

Figure 31: Mode frequencies variation (left); Maximum deflection variation (right) with Theta

3.3.1.4 Cantilever Thickness

Table 9 shows the variation in mode frequencies at different w_c (cantilever thickness).

Table 9: Mode frequencies at different cantilever thickness

w_c (μm)	$L_e (\mu m)$	d_z (μm)	Mode1(Hz)	Mode2(Hz)
32	126	0.629	690.6	2603.5
24	126	0.632	697.1	2497
16	126	0.639	702.9	2354
8	126	0.662	704.7	2061.3
4	126	0.705	695.9	1657.6

Maximum deflection is not much affected by the cantilever thickness till w_c= 16 μm as shown in Figure 32 (right) , but at w_c= 8 and 4 μm, the d_z seems to increase. Generally, d_z should not be affected by the change in cantilever width, but the variation could be the contribution of bending effects at smaller cantilever width such as w_c= 8 and 4 μm. Figure

33 shows the mode 2 resonance shapes of the structure at w_c= 4, 8 and 16 μm. As expected, the mode 2 frequency increases as a result of increased cantilever stiffness in the y-direction.

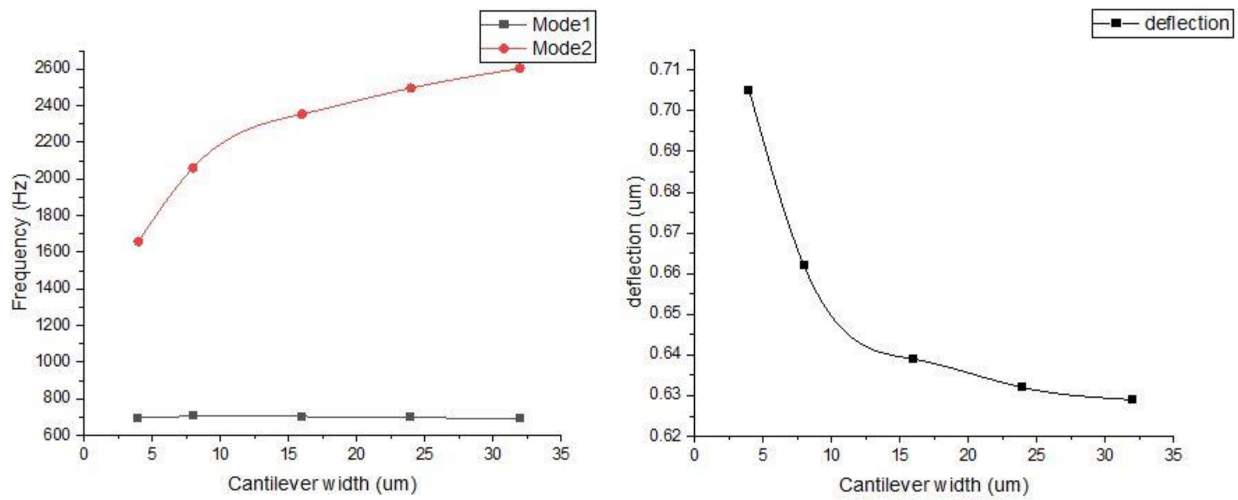

Figure 32: Mode frequencies variation (left) with theta; Maximum deflection variation (right) with Theta

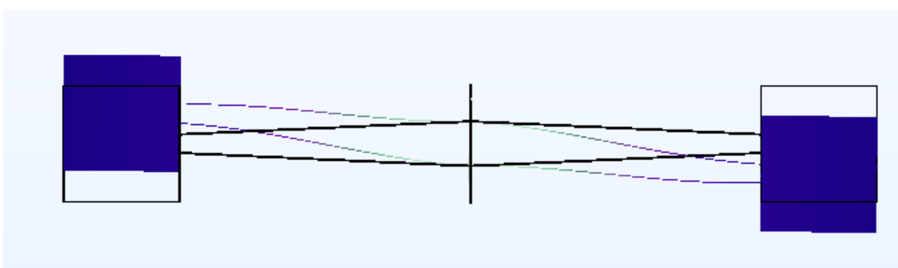

(a)

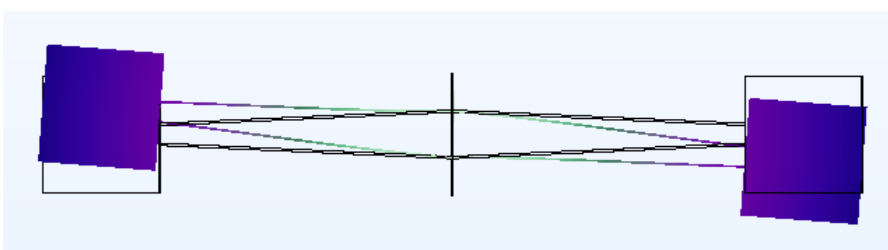

(b)

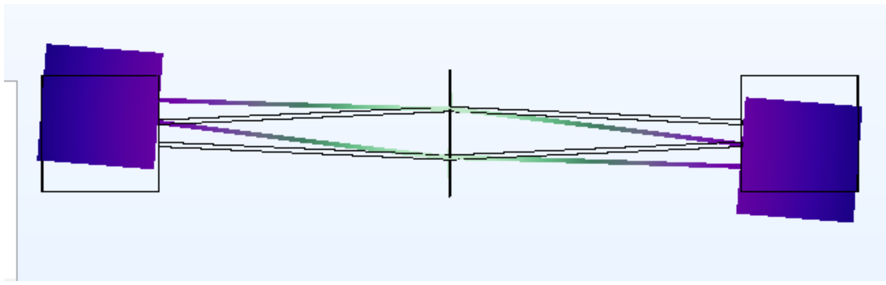

(c)

Figure 33: Mode 2 shapes of structure at (a) w_c= 4;(b) w_c= 8;(c) w_c= 16

Though at lower cantilever width there is gain in d_z, still the structure suffers from the unwanted sideways movement as shown in Figure 33(a). Hence, cantilever thickness 16 μm and above is recommended. There is a slight fall in mode1 frequency as result of reduced mass of cantilever.

To summerize, the maximum deflection depends on the effective length of the spring (given width and thickness is constant). A slight increase θ can significantly reduce the sideways movement in y-direction. Though increasing the thickness of the cantilever beams also increases the mode 2 frequency, but it also affects the mode1 frequency because of the increase in mass of the cantilever. Cantilever beams could be unpredictable at lower widths.

One can get the desired deflection by only changing the effective length of the spring. The structure can be made stiffer in the y-direction by the combinations w_c and θ. Maximum deflection of 0.632 with plate side of 400 μm could give maximum change in capacitance of more than 200 fF. Calculation for the same is provided in section 3.7. To avoid risk and for better stability, it is recommended to fabricate sensors with 24 and 16 μm width of cantilever beams.

To improve the performance of the structure with cantilever width of 8 μm, a couple of cantilever designs are tested (as shown in Table 10) with the same configuration as Table 8. One of the designs is like the original design except the cantilevers are now joined with parallel beams. The second design is based on bridge-type design. Both designs have nearly the same maximum deflection as of original design. There is little difference in mode 1 resonance frequencies of all the designs, bridge design has the lowest because of extra mass between the cantilevers. This design also has the highest mode 2 frequency. Hence, it can be a better design at lower cantilever width. Incorporation of these design may slightly improve the stability, but extra added mass may increase the gravitational effect. In addition, they may present more resistance to the airflow in comparison to the original design. Hence, these designs may not improve the overall performance of the sensor.

Table 10: Cantilever designs to improve the sideways movement or Mode2 resonance frequency.

Design	Maximum Deflection (μm)	First two mode frequency (Hz)
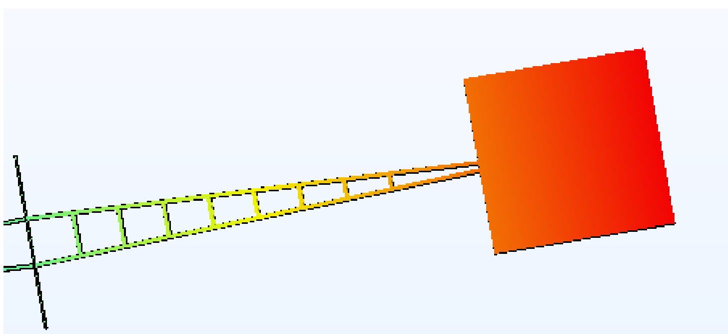 (a) Design with joiners	0.662	Mode 1= 702 Mode 2=2163
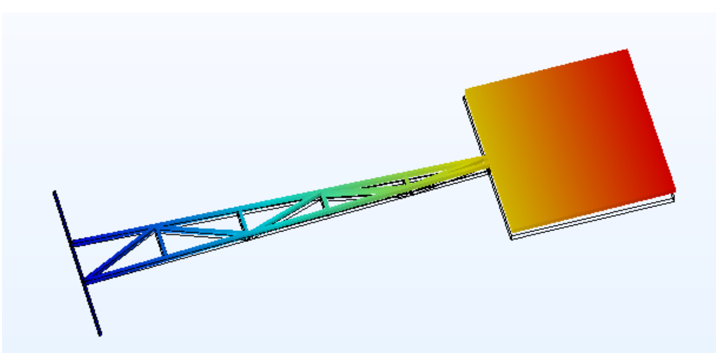 (b) Cross bridge Design	0.661	Mode 1= 699 Mode 2=2203

3.4 Effect of Gravity

When no flow is applied the structure would bow down due to gravity. Hence, it is necessary to make sure that the deflection is marginal with respect to the deflection.

$$weight\ of\ the\ plate = Density\ of\ silicon \times volume\ of\ plate = \quad 93.16\ nN \qquad 3.8$$

The deflection of the plate after applying gravitational force in z-direction on both the plate comes out to be 0.0032 μm as shown in Figure 34, which is < 1% of the maximum deflection. Similarly, the effect of gravity is analyzed in the x-direction, Figure 35 shows the displacement of the structure due to gravity. The displacement of the spring is 0.0014 μm which is <0.5 % of total deflection.

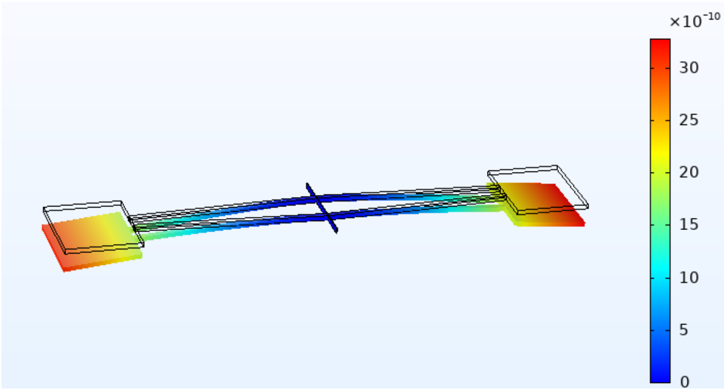

Figure 34: Deflection due gravity on Z-direction.

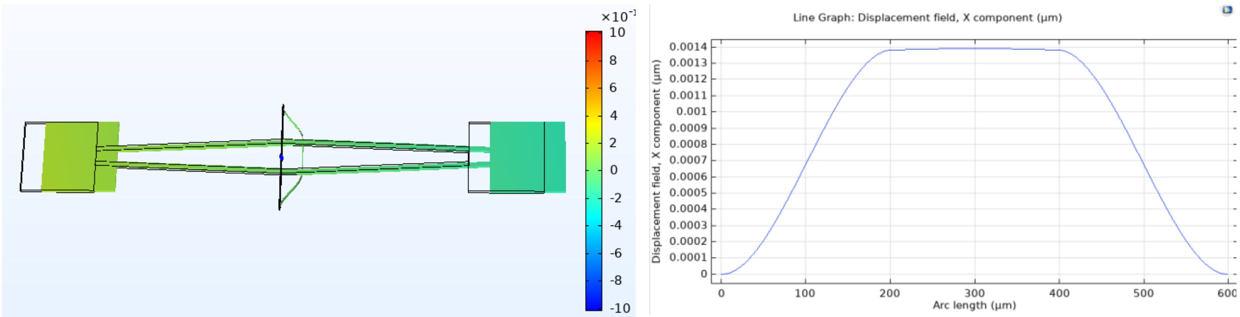

(a) (b)

Figure 35:(a)Effect of gravity in x-direction;(b) Displacement of spring

3.5 Stress Analysis

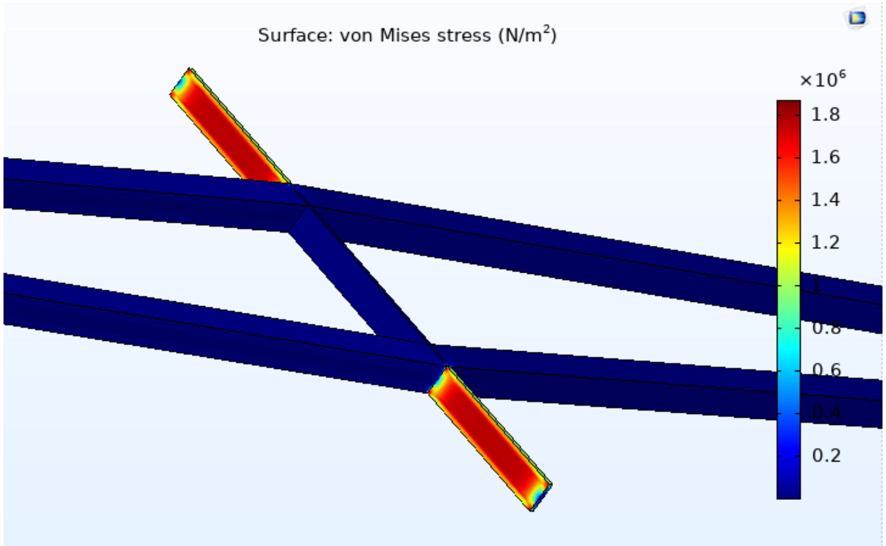

Figure 36:Plot showing von Mises stress in the structure.

The von Mises yield criterion states that if the von Mises stress of a material under load is equal or greater than the yield limit of the same material under simple tension, the material will yield [57]. Ultimate tensile strength (UTS) is taken as the maximum stress before facture, and the UTS of <100> silicon experimentally found to b 350 MPa [58].

In this design, the torsional spring is in maximum stress below 2MPa (far below UTS of silicon) as shown in Figure 36.

3.6 Torsional spring constant calculations

In this section, the Torsional spring constant calculations will be compared with simulated result. A few approximations to calculate tortional spring constant are available in the literature and it is perplexing to differentiate which approximation is accurate and better. In this section, different approximations, available in the literature, will be analysed on the basis of accuracy and conditions. This could also be helpful specially in designing tortional springs isong cantilevers.

3.6.1 Approch1: Roark's Formula [56]

The torsional spring constant can be calculated for effective length L_e of 126 μm by equation *3.6*. The value of K for $\mathrm{b} = 4\ \mu m$ and $\mathrm{a} = 25\ \mu m$ has been calculated and given by *3.7* as $K = 479.6 \times\ 10^{-24} m^4$. The sheer modulus for isotropic silicon can be calculated by following equation *3.9* [59]. Roark's formula is valid for both isotropic and anistropic silicon. It clearly explains the difference between K and polar moment of inertia. Properties of isotropic silicon taken in COMSOL Multiphysics simulations are given in Table 11.

$$G = \frac{E}{2(1+v)} \tag{3.9}$$

Table 11: Properties of Isotropic silicon taken from COMSOL Multiphysics5.4

Properties of Isotropic silicon	Values
Young's Modulus (E)	170Gpa
Poisson's Ratio (v)	0.28
Shear Modulus (G) (from eq. *3.9*)	66.4Gpa

Putting all the required values to calculate the torsion spring constant in equation *3.6* gives.

$$K_t = 2.53 \times 10^{-7}\ Nm. \tag{3.10}$$

3.6.2 Approach 2 : Eddie et al. [60]

Eddie et al.[60] presented the concept and design of torsional micro-mirrors systems and defined torsional spring constant as:

$$K_\theta = \alpha \frac{Gwt^3}{3L} \quad 3.11$$

Where G is shear modulus, w is width, L is the length and, t is the thickness of the spring. α is a correction factor. The literature does not provide much information about α and takes $\alpha = 1$ for the calculations. Using $\alpha = 1$ and putting all the required values in equation *3.11.* The torsional spring constant K_θ is given by:

$$K_\theta = 2.81 \times 10^{-7} Nm \quad 3.12$$

3.6.3 Approach 3 Green et al [61]

According to [61], the torsional spring constant for an isotropic material can be calculated by equation

$$K_\phi = K_z \frac{2L^2}{3(1+\upsilon)} \quad 3.13$$

Where, K_z is the normal spring constant as shown in Figure 37, υ is Poisson's ratio and, L is the length of the spring. N is the force applied in Z-direction or normal to the cantilever.

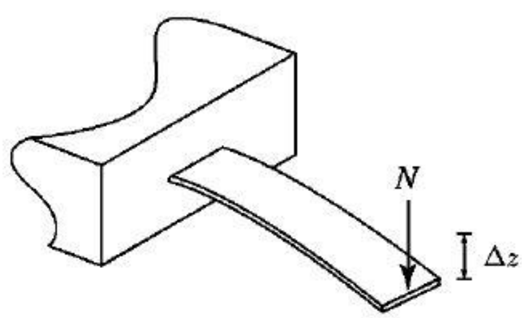

Figure 37: Schematic to illustrate the normal spring constant [59].

Normal spring constant K_z can be calculated from 3.14 [61]

$$K_z = \frac{Eh^3b}{4L^3} \tag{3.14}$$

Where h, b, L are the height, width, and length of the cantilever, respectively. Inserting all the values in equation *3.14* gives:

$$K_z = 33.99\, N/m^2 \tag{3.15}$$

Using equation *3.15* in equation *3.13* gives torsional spring constant K_ϕ as:

$$K_\phi = 2.81 \times 10^{-7} Nm \tag{3.16}$$

The spring constant from formula 2 and formula 3 is the same, which should not be a surprise. As putting the formula of K_z (eq *3.14*) into equation *3.13* gives

$$K_\phi = \frac{Eh^3b}{4L^3} \times \frac{2L^2}{3(1+\upsilon)}$$

$$K_\phi = \frac{E}{2(1+\upsilon)} \times \frac{h^3b}{3L}$$

Where, $\frac{E}{2(1+\upsilon)}$ can be replaced by shear modulus according to equation *3.9*. Now, K_ϕ can be written as:

$$K_\phi = \frac{Gh^3b}{3L} \tag{3.17}$$

For $\alpha = 1$, Equations *3.11* and *3.17* are the same. Thus, the value of spring constant. This resemblance also verifies the *G* for isotropic material is given by equation *3.9*.

3.6.4 Approach 4: Kwak et al. [62]

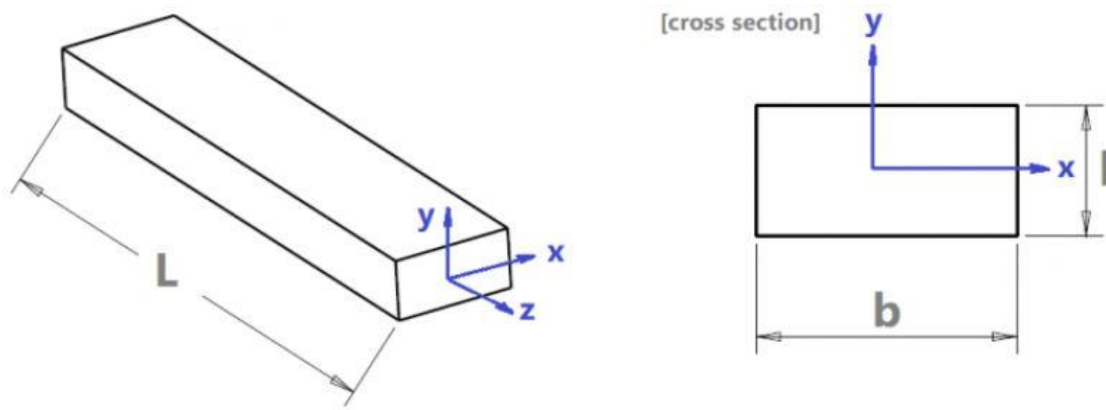

Figure 38:: Schematic view of rectangular cantilever (left) and cross-section (right) [61]

The torsional spring constant K_t is defined as in Equation 3.18 and is proportional to the bulk shear modulus G_{Bulk} , Boundary condition constant α, polar moment of inertia I_p and, inversely proportional to the length of spring L [62].

$$K_\psi = \left(\frac{G_{Bulk} I_p}{L}\right) \tag{3.18}$$

I_p for a rectangular cross-section as shown in Figure 38 [63] can be given by :

$$I_p = bh\left(\frac{b^2 + h^2}{12}\right) \tag{3.19}$$

Putting the value of b and h according to the design in 3.19 gives:

$$I_p = 574.1 \times 10^{-24}\, m^4 \tag{3.20}$$

Putting value of G_{Bulk}, I_p and, $L = 126\ \mu m$ in equation *3.18* gives:

$$K_\psi = 3.02 \times 10^{-7}\, Nm \tag{3.21}$$

3.6.5 Comparison between Approaches

The value of torsional spring constant, according to the FEA simulation for parameters given in Table 6, is calculated as:

$$K_s = 2.74 \times 10^{-7}\, Nm \tag{3.22}$$

Table 12: Error Analysis for Formulas

Approach	Value	% error= $\left(\frac{K_s - K_{formula}}{K_s}\right)$
Roark's Formula [56]	2.53×10^{-7}	0.076
Eddie et al. [60]	2.81×10^{-7}	0.025
Green et al [61]	2.81×10^{-7}	0.025
Kwak et al. [62]	3.02×10^{-7}	0.102

Table 12 gives the % error in each formula. The error for all the formulas is less than one percent except Approach 4 as it considers polar moment of inertia, in contrast to Roark's formula, which only includes a fraction of polar moment of inertia and called K, as discussed in section 3.2.2. It is also important to note that Approach 2 and Approach 3 will be valid for isotropic materials only. The value of the simulated torsional spring constant agrees well with the theoretical calculation within the error of <1%.

3.7 Capacitance Calculations

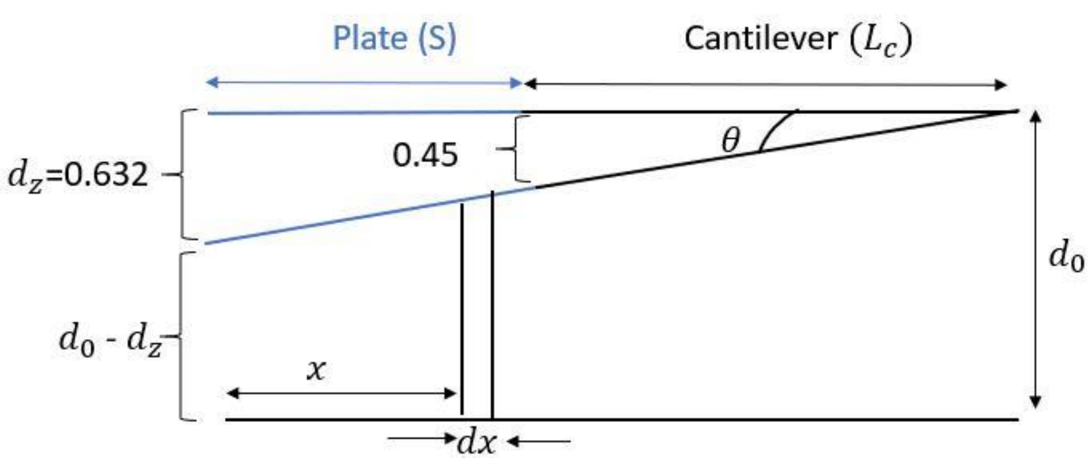

Figure 39:schematic side-view of the plate (blue) and cantilever (black) after deflection.

The side-view of the plate (blue) and cantilever (black) at maximum deflection is shown in Figure 39. The length of the cantilever is L_c and side of the plate is S. Assume an infinitesimal element at a distance x of length dx. The capacitance corresponding to that element can be written as:

$$dC = \frac{A\varepsilon}{d}$$

where, $A = dx \times S$, $d = (d_0 - d_z) + x\, tan(\theta)$ and, $tan(\theta) = \frac{0.632-0.45}{400} = 0.182$

$$dC = \frac{S\, \varepsilon\, dx}{(d_0 - d_z) + x\, tan(\theta)}$$

By Integrating,

$$C = \int_0^S \frac{S\, \varepsilon\, dx}{(d_0 - d_z) + x\, tan(\theta)}$$

$$C = S\, \varepsilon \left[\frac{\ln((d_0 - d_z) + S\, tan(\theta)) - \ln(d_0 - d_z)}{tan(\theta)}\right]$$

$$C(\theta) = \frac{S\, \varepsilon}{tan(\theta)} \ln\left[\frac{d_0 - L_c\, tan(\theta)}{d_0 - (S + L_c)\, tan(\theta)}\right]$$

$$C = \frac{S\, \varepsilon}{0.182} \left[\ln \frac{1.55}{1.368}\right]$$

$C = 972 \times 10^{-15}\, F$ or,

$$C = 972\, fF \tag{3.23}$$

The capacitance between the plate and the substrate when there is no deflection is given as:

$$C_0 = 708\, fF \tag{3.24}$$

Change in Capacitance at maximum deflection = $C - C_0 = 264\, fF$.

3.8 Pull-in Voltage Calculation

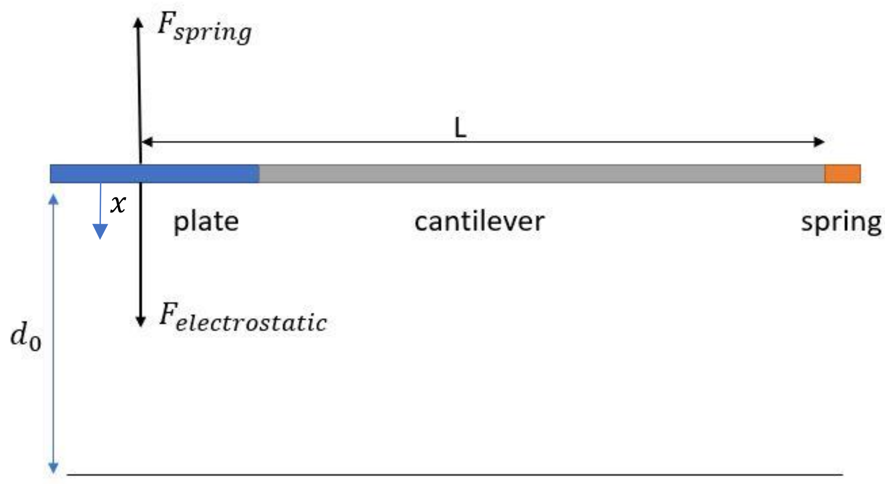

Figure 40: Side-view of the sensor indicating forces acting on the plate.

Voltage *V* is applied and at static equilibrium:

$$F_{electrostatic} = F_{spring}$$

Also,

$$\tau_{electrostatic} = \tau_{spring}$$

Where, τ is torque,

$$F_{electrostatic}\, L = K_t\theta$$

Assuming parallel plate approximation,

$$F_{electrostatic} = \frac{\varepsilon A V^2}{2\,(d_0 - x)^2}$$

Inserting $F_{electrostatic}$ in torque equation,

$$\frac{\varepsilon A V^2}{2\,(d_0 - x)^2}\,\mathrm{L} = K_t\theta$$

$$V = \sqrt{\frac{2K_t\theta\,(d_0 - x)^2}{\varepsilon A}} \qquad 3.25$$

The maximum of voltage is obtained for :

$$\frac{dV}{dx} = 0$$

$$x = \frac{d_0}{3}$$

Inserting x in eq. 3.25 :

$$V_{Pull-in} = \sqrt[2]{\frac{8K_t d_0^3}{27\epsilon A L^2}} \qquad 3.26$$

Where, K_t is torsional spring constant, d_0 is the initial distance between the plate and the substrate as shown in Figure 40, A is the area of the plate and cantilevers. Cantilevers also form capacitance with the substrate, thus it is included to calculate the $V_{Pull-in}$ .Inserting the value of $K_t = 2.74 \times 10^{-7}\ Nm$ (from FEA simulation) , $d_0 = 2\mu m$ and other required values in equation 3.25.

$$V_{Pull-in} = 0.79\, Volts \qquad 3.27$$

The pull voltage obatined from equation 3.26 has been calculated using parallel plate approximation or to calculate $F_{electrostatic}$, it is assumed that the plate is parallel to the substrate. The pull-in voltage can also be calculated using numerical approach using standard transducer science theory. τ_{ext} can be given by equation *3.28* [64]. Equation *3.28* can be solved numerically as shown in Figure 41. At zero volts τ_{ext} is linear function of θ and slope simply represents mechanical spring. As voltage increases the structure will rotate and the equilibrium position (point where $\tau_{ext} = 0$) shifts towards right.

$$\tau_{ext}(V,\theta) = \frac{V^2\, C(\theta)^2}{2}\frac{d(1/C(\theta))}{d(\theta)} + K_t\theta \qquad 3.28$$

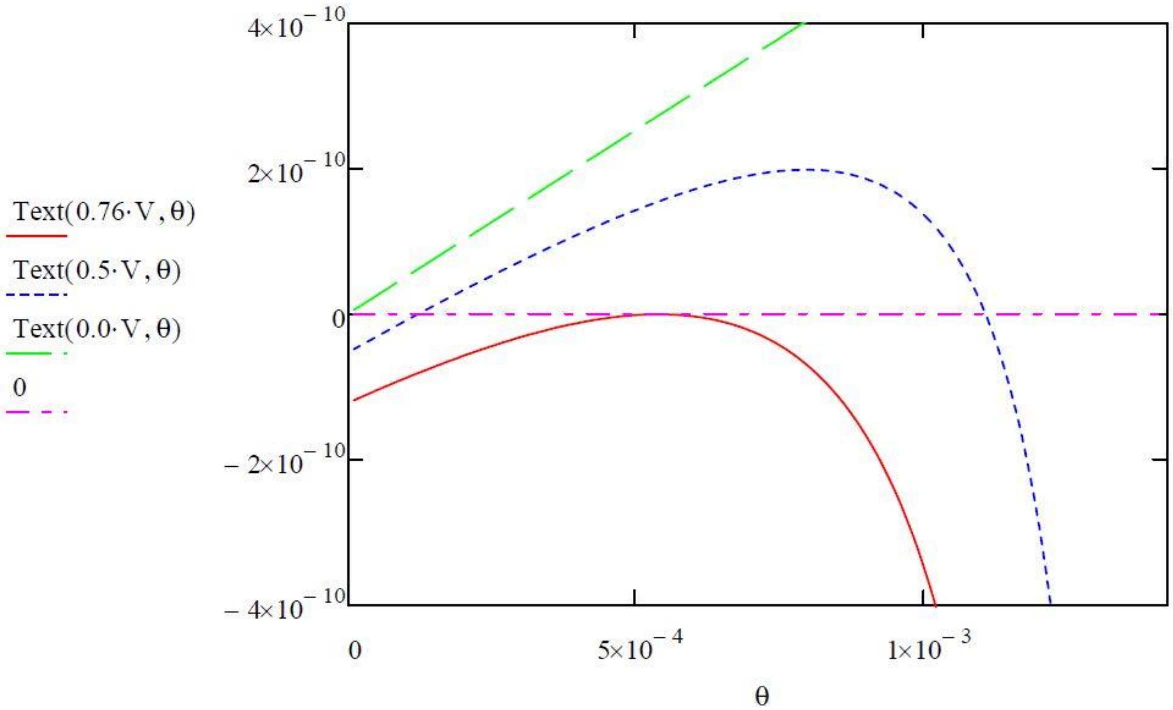

Figure 41: Plot showing τ_{ext} as a function of θ

At voltage 0.76, there is no equilibrium. Thus, the structure will be pulled in.

$$V_{Pull-in}(numerically) = 0.76\, Volts$$

The pull-in voltage is very low to use signal conditioning circuits to obtain the capacitance change like AD7747, which works at 2.7-5 volts. Hence, it is important to investigate how to increase the pull-in voltage or another method to do measurement with the device. From equation *3.26*, K_t, A and, L can be used to change the pull-in voltage but it comes at the cost of sensitivity. L has a greater impact on the $V_{Pull-in}$ because of $1/_L$ dependence. Hence, L can be the most effective parameter to improve the $V_{Pull-in}$. One of the solutions could be to reduce the L or bringing the plate on left side towards the torsional axis and balancing using dummy mass (as shown in Figure 42). The substrate under the dummy mass needs to be removed so that it does not form any capacitance with substrate. The cost is the reduction in deflection of the plate or sensitivity. Another solution could be increasing length of the cantiver (which is supposed to be in the flow) and using another paddle to counteract the electrostatic force as shown in Figure 42.

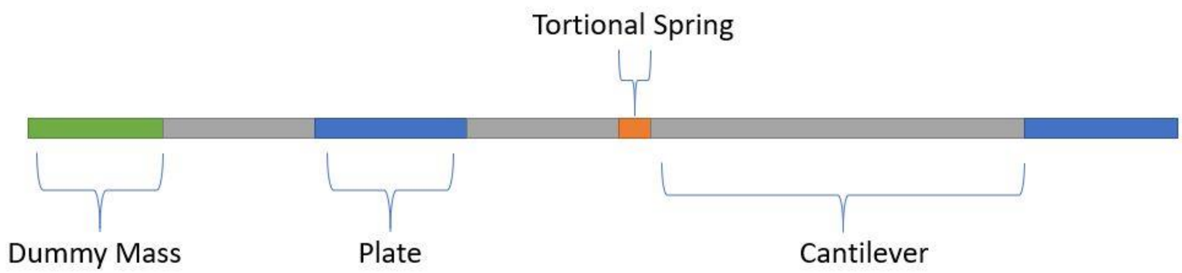

Figure 42: Side view of the design (including dummy mass to balance)

The pull-in voltage can be improved without reducing the sensitivity. Though, the longer cantilever would increase the deflection due to gravity and put more stress in the torsional spring, but these limits can be pushed as shown in section 3.4 and 3.5. The stress on the torsional spring is 2MPa (with current design) which is far below the maximum stress before failure (350 MPa). The deflection due to gravity (with current design) is ≪1% of total deflection.

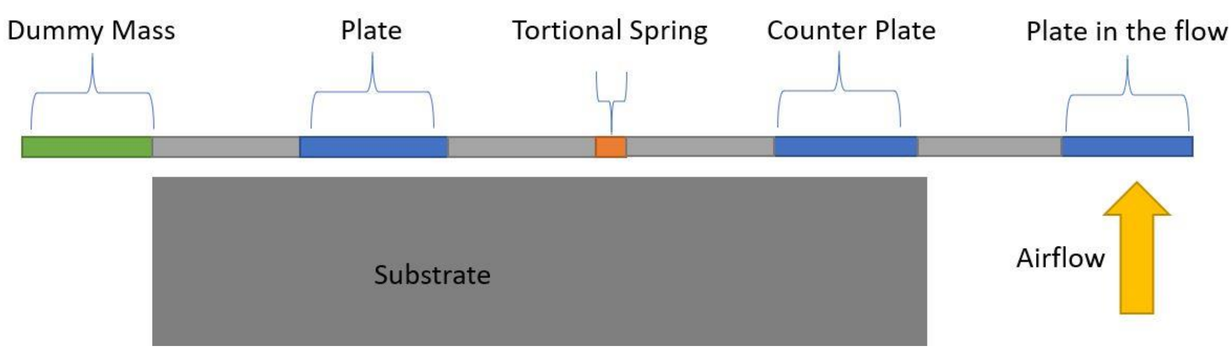

Figure 43: Side of design to improve pull-in voltage.

Dedicated electronics could also be designed to measure the capacitance with lower pull-in voltage (similar to shown in Figure 44). The V_{in} signal should be less than pull-in voltage (Lets say 100 mv).

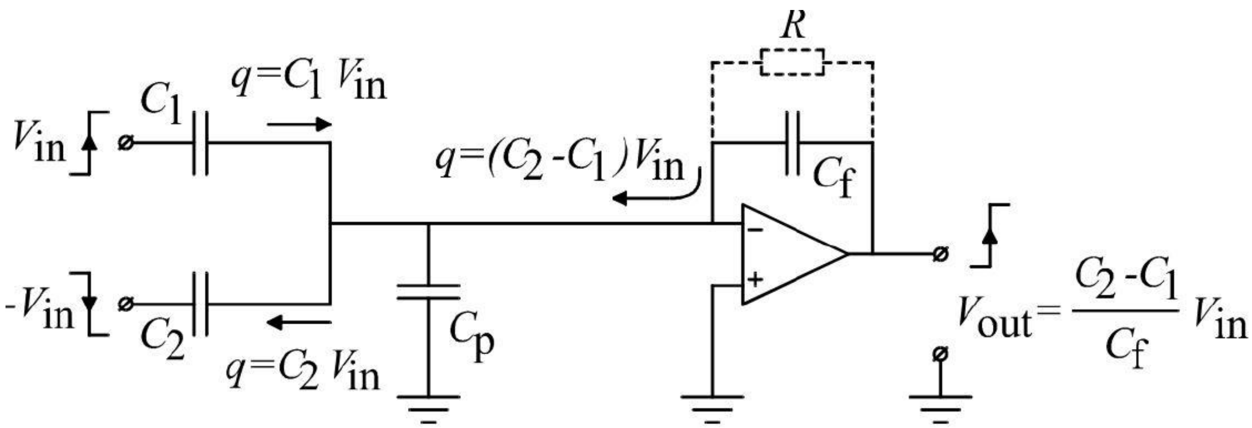

Figure 44: Capcitance calculation using charge amplifier.

3.9 Mask Designing

The mask for the fabrication is designed in CleWin5.4. The major components of the mask has been mentioned in Figure 45. Close-up view of device, reference capacitor and handle layer (HL) trenches around the plate is shown in Figure 46, Figure 47(b) and Figure 47(a) respectively.

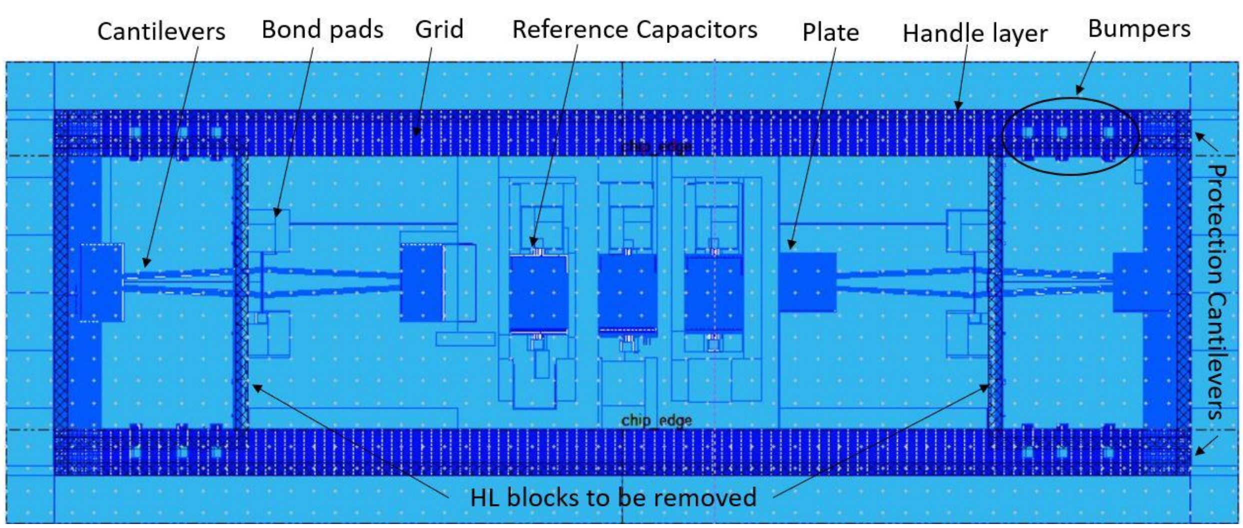

Figure 45: Top view of the fabrication mask.

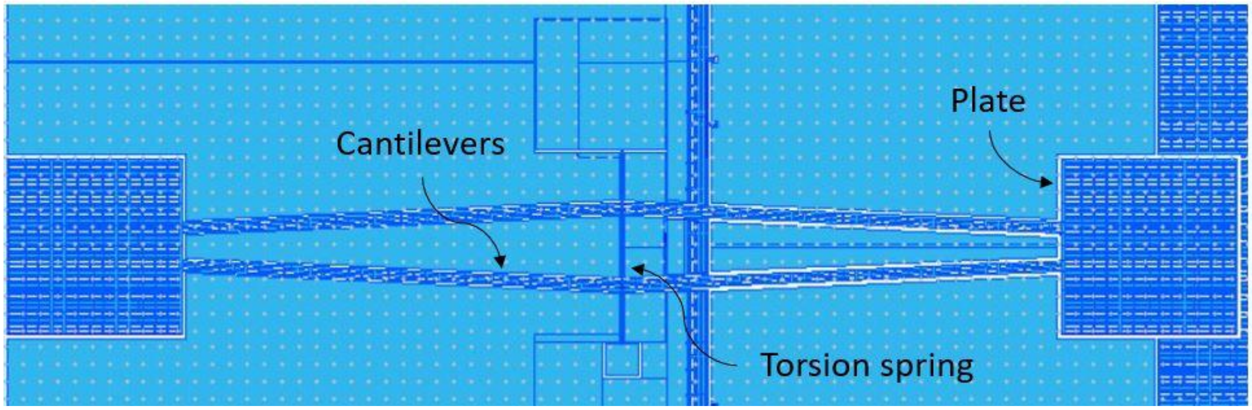

Figure 46: Close-up view of device (from Mask Design)

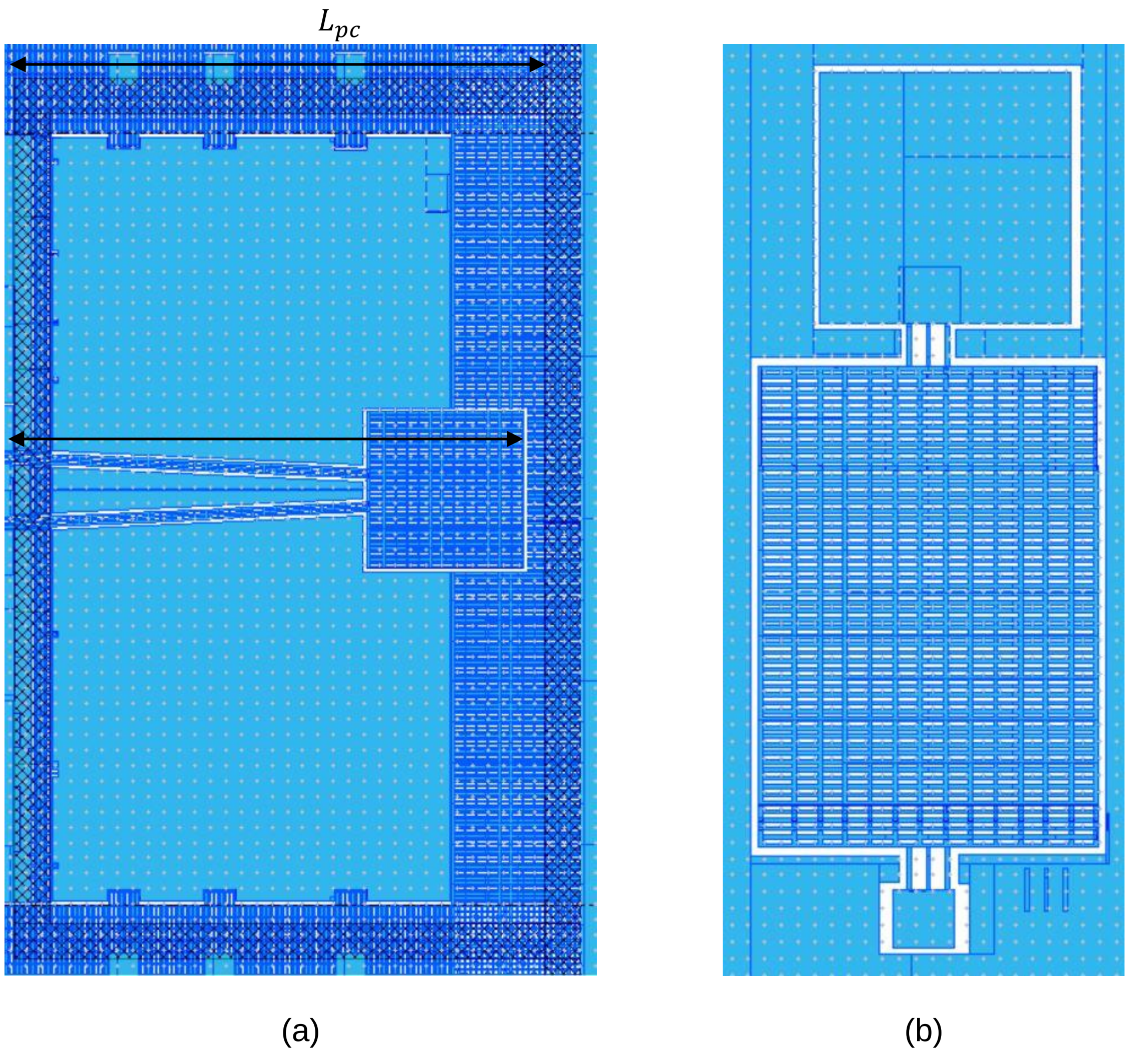

Figure 47: Close-up view of (a) HL trenches around plate;(b)Reference Capacitor, (from Mask Design)

For variation, the dimensions of the plate is changed to 300 $\times$ 534, keeping the area of plate constant. Protection cantilevers are designed to protect the paddle from touching other objects. Thus, the cantilevers are extended a bit more further than the paddle or the length of the protection cantilevers (L_{pc}) is larger than the sum of length of device cantilever and plate (clear from Figure 47(a)).

The reference capacitors include the parasitic capacitance offered by the cantilevers in the device. The size of bond pads in reference capacitor and the device is same to include the parasitic capacitance offered by the bondpads. The second bond pad is made smaller (50 $\times$ 50 μm^2, whereas bigger bond pad is 300 $\times$ 300 μm^2) to reduce overall parasitic capacitance. One can also use silicon nitride insulation to reduce the parasitic capacitance in a way as shown in Figure 48, but in this case, parasitic capacitance offered by smaller bond pad (0.0432 pF) is nearly equal to the parasitic capacitance offered with the use of silicon nitride (0.0442 pF), reason being the high dielectric constant of silicon nitride (ε_r=9.5). In addition, silicon nitide has thermal coefficient different than silicon, which could introduce thermal dependence. It also has tensile stress after deposition, which might give tension in torsion spring. Thus, the silicon nitide is not used in fabrication.

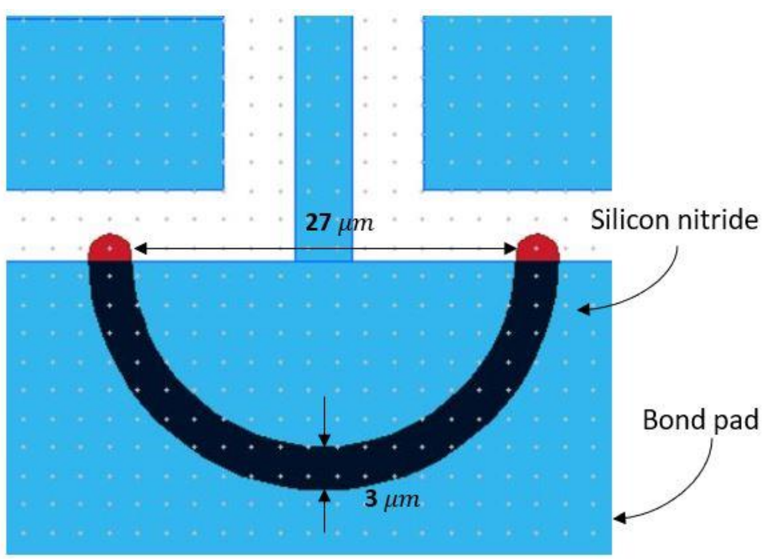

Figure 48: Silicon nitide insulation to reduce the parasitic capacitance

3.9.1 Design Rules

Design rules necessary to know in order to understand the designing of the mask [54].

3.9.1.1 For Device layer

- The minimum feature size of the design should be greater than 3.5 μm, smaller than this may be reproduced accurately.
- The underetched box layer will be of the order 5 to 10 μm. Thus, to release the structure from the substrate, make sure thatany part should be less than 10 μm.
- Parts that should remain fix to the substrate such as bond pads should have width no less than 50 μm

3.9.1.2 For Handle Layer

- Handle layer are used to release the chips by etching trenches that are 90 μm wide. Trenches less than 90 μm may not reach the BOX layer.
- 90 μm trenches will reach the BOX layer with a width anything between 40 and 200 μm.
- While etching trenches in the handle layer make sure to have device layer over it because the BOX layer is only 2 μm thick and can not withstand the pressure between front and back during etching.

Figure 45 shows the top view of the mask. The dimension of the chip is 8995 $\times$ 3370 (in μm). Only etch 90 μm wide trenches can be etched and we need to remove the handle layer beneath the plate or paddle. Thus, the devices are made on the left and right edges of the chip to make it easy to remove the handle layer beneath the devices. In middle, three reference capacitors are drawn with slight variation in the capacitance of all three so that the one most near to the plate capacitance can be used while measurement. For variation, a device on the left of the chip has a rectangular plate, unlike the right one which has a square plate with the same area.

One of the challenges is to remove the handle layer block beneath the sensing plates. To do so, 90 μm wide trenches has been drawn around the plate as shown in Figure 45 and

Figure 47(a). The falling block should not move in any other direction or the sideways or upward movement of the block needs to be restricted, otherwise it may destroy the sensing paddle. To avoid sideways movement, bumpers are designed (as circled in Figure 45, the enlarged view is shown in Figure 49 (a)) to make sure the piece of handle layer should not go upwards of sideways during the MEMS fabrication. It is very important to imagine the device as 3D to understand the designing of the bumpers and handle layer trenches. The trick to remove the block worked well and the device is successfully fabricated in clean room.

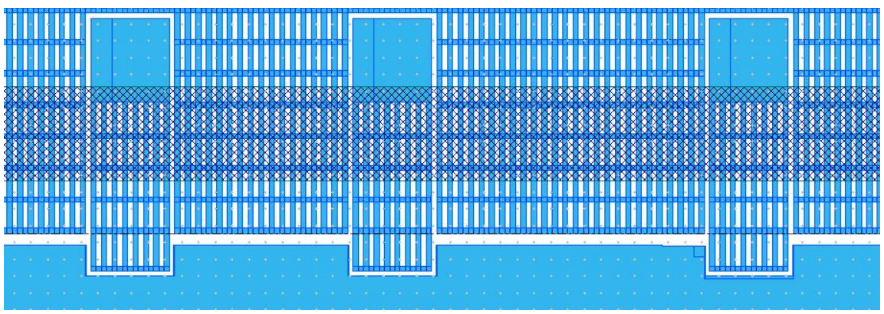

(a)

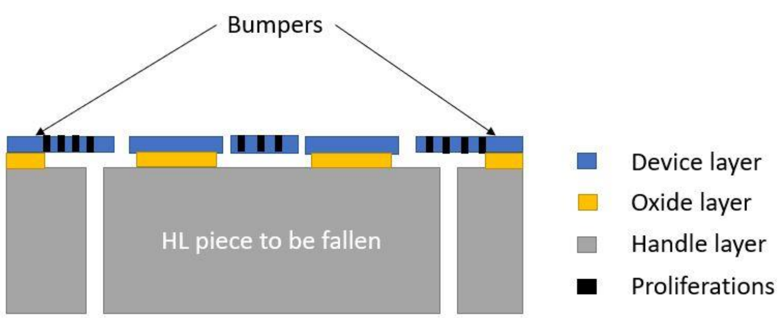

(b)

Figure 49: (a) enlarged view of bumpers;(b) sideview showing bumpers.

Chapter 4: Measurements

With the designing of fabrication masks, the device is fabricated in MESA^{+} lab at the University of Twente. Before the device comes out of lab, there is need to design test setup to perform the measurrements. The idea is to get a repeatable flow and velocity profile from the test setup with the help of commercially purchased anemometer to caliberate the fabricated device with the help of obtained results.

After thorough search on commercially available anemometer, Voltcraft's PL-135 (see Figure 50) is chosen to perform measurement on test setup. The specifiations and the dimensions of the sensor is given in Table. The search was based on accuracy and functionality the sensor provides in least cost. The chosen anemometer also measures the temperature.

Figure 50: Voltcraft's PL-135 anemometer sensor

Table 13: Specifications of Voltcraft's PL-135 anemometer sensor

Wind speed resolution	0.01 m/s
Accuracy	5%
Max. Air speed	25 m/s
Min. Air speed	0.1
Power supply	USB/3.7 V Li-Po battery
Height	27 mm
width	58mm
Temerature reading range	0-50

4.1 Test Setup

Test setup comprises of a cylindrical transparent tube of length 1m and inner diameter 11.4 cm with fan fixed at one end whose fan is controlled by varying voltage as shown in Figure 51. The tube is tightly filled with straws of diameter 6 mm and length 12.5 cm each. The idea is to let the flow fully developed in the straws. To do so, first we need to calculate the Reynolds number for the straw. Lets assume the velocity inside the straw is 0.5 m/s, the Reynolds number can be calculated by equation *4.1* as 202.7. The flow regime is laminar as $R_e < 4000$. Thus the entrance length can be computed using equation 4.1 [65]:

$$\frac{L_h}{D} \approx 0.06R_e \tag{4.1}$$

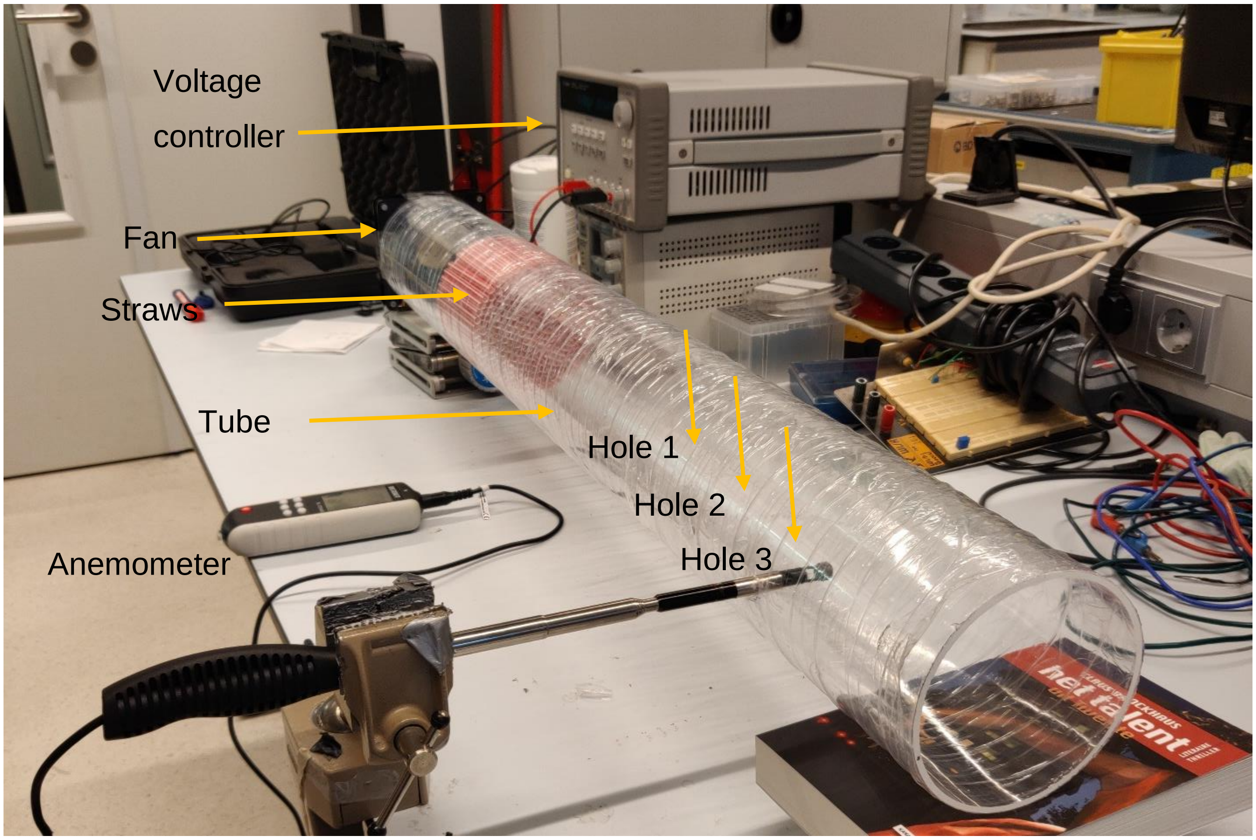

Figure 51: Experimental setup to investigate the flow profile.

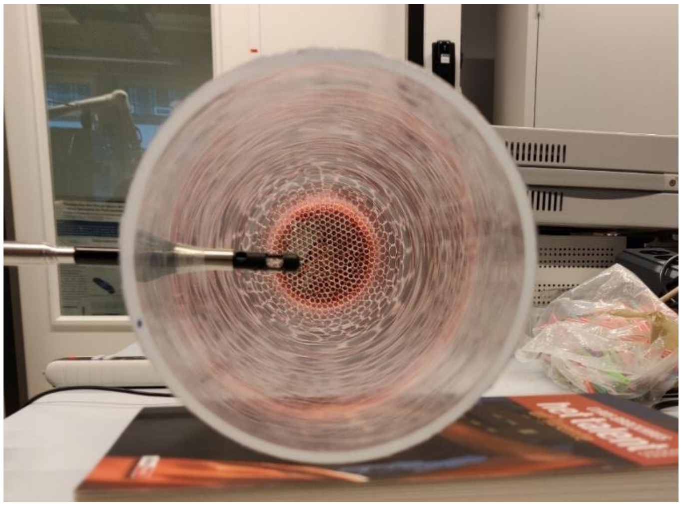

Figure 52: Side-view anemometer inserted into one of the holes.

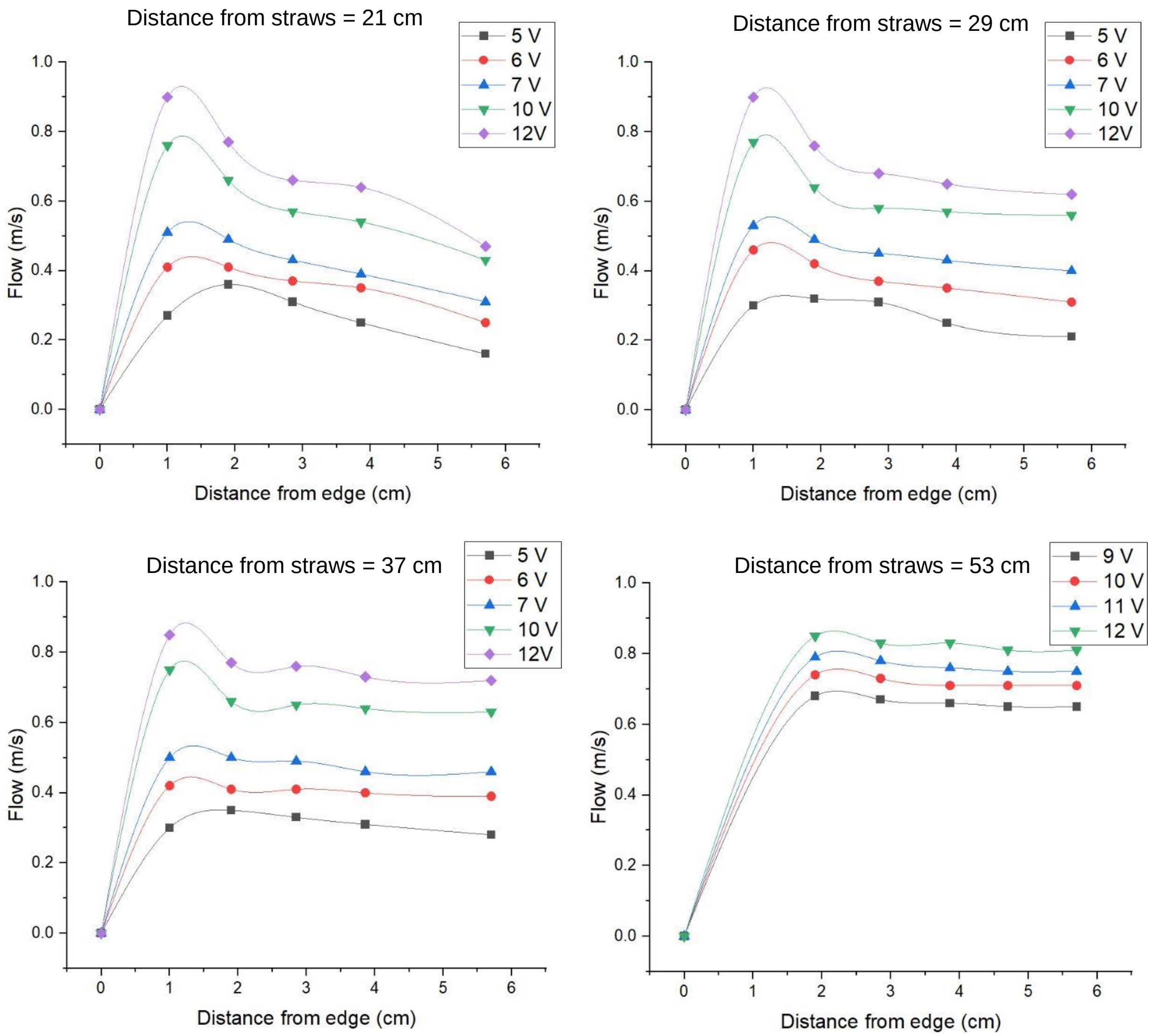

Figure 53: Velocity profile at various voltage at (a) Hole 1; (b) Hole 2; (c) Hole 3;(d) Velocity profile after shifting of straws for hole 3

The entrance length for straws is 12.16 cm. similarly, for laminar flow, the entrance length for cylindrical tube can be calculated at 0.5 m/s as 1.365 m.

In a cylindrical pipe of uniform flow Q, flowing full, the pressure drop Δp can be called by Hagen- Poiseulli equation [66].

$$\Delta p = \frac{8\mu LQ}{\pi R^4} \qquad 4.2$$

Where, μ is dynamic viscosity, R is radius, L is the length. The pressure drop in straw at 1 m/s is $\Delta p_s = 0.5\ Pa$, where as pressure drop in the tube is $\Delta p_s = 0.04\ Pa$. The pressure drop in straws is quite significant. Thus, the homogenous flow is expected in the straws.

Three holes are drilled in the tube at a gap of 8 cm, first being drilled at 21 cm from the end of the straws. The anemometer is displaced into these holes to read the velocity at different locations along the radius as shown in Figure 52. The velocities are recorded at 5, 6, 7, 10 and 12 V with the anemometer. The plot of velocity along the radius is shown in Figure 53.

Following observations are recorded during the experiment:

- Lot of fluctuation in velocity reading at low flows compared to flow at higher voltages.
- The velocity profile tend to flatten from hole 1 to hole 3.
- Velocity data near the edge of the tube is not completely reliable because of the possibility of pressure leak due to the uneven diameter of the probe at the tip.
- The variation in the velocity is minimum at the third hole which could mean that the parabolic velocity profile is starting to develop. Hence, reading can be taken by shifting the straws further to the left.

Possible causes of fluctuations and errors in the graphs:

- A bit of pressure leak from the measuring hole.
- Noise of fan and other machines in the lab. To see the effect of external noise, measurements could be taken without the flow.

Taking account of observations, it is expected that the velocity profile would become more flat and might develop into parabolic profile further away from the straws. Thus, the straws are shifted by 16 cm and another measurement is taken at hole 3 at 9, 10, 11 and 12 V and the result is plotted as Figure 53(d). The velocity profile become more flat than previous profile for hole 3.

As expected the flow is quite homogeneous inside the tube .It is recommended to use high voltage > 8 volts to reduce fluctuations and increase repeatability in the reading of anemometer. Due to time limitation, the possible causes of fluctuations and errors have not been explored.

4.2 Device Measurements

Few samples of the device are analyzed using white light interference. Figure 54 and Figure 55 show the measurement results for sample1 and sample2 respectively.

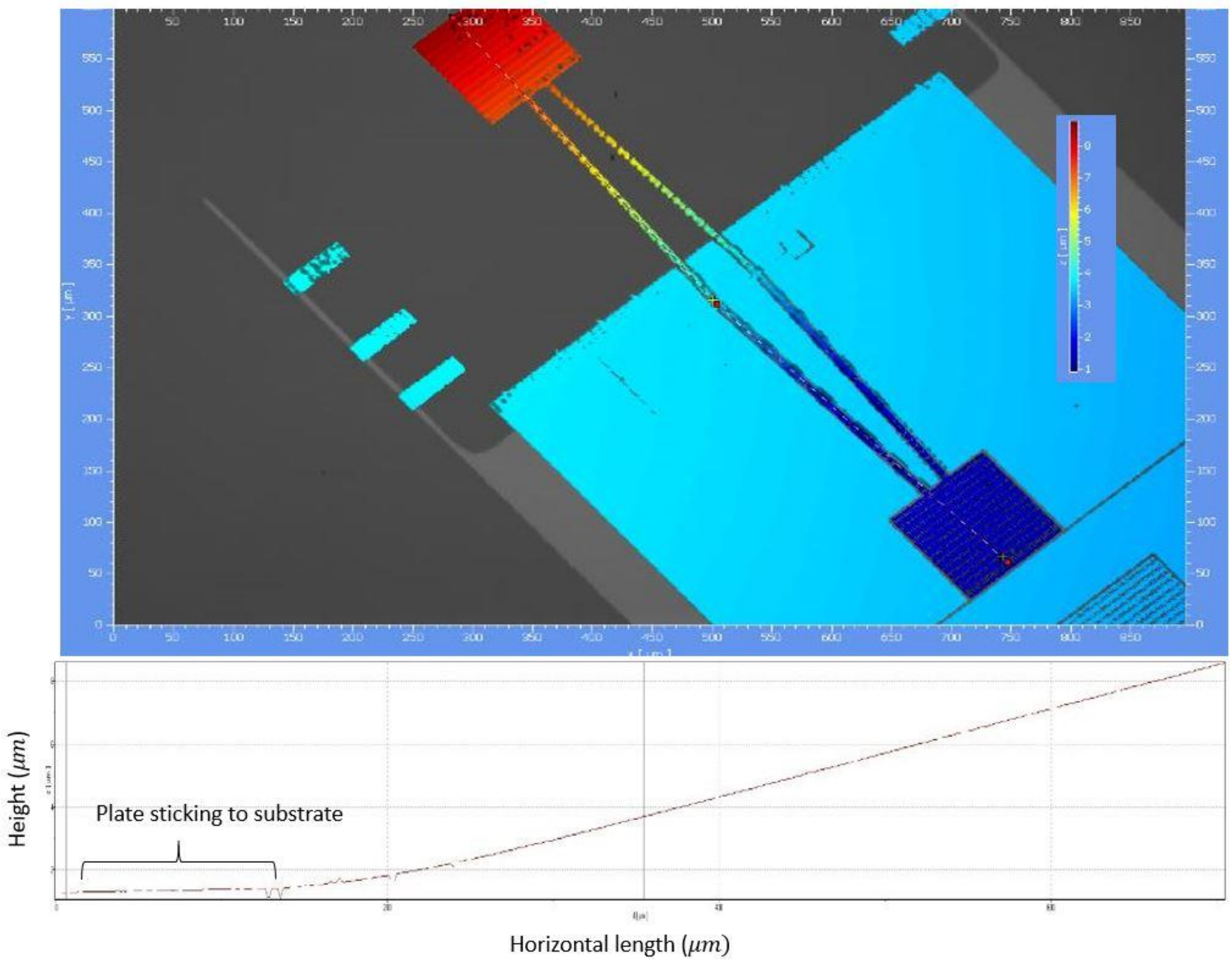

Figure 54: White light interfernce results for sample 1

In sample1, plate is stuck to the substrate as shown in Figure 54, whereas in sample2, only tip of the plate is stuck to the bottom or substrate. Sample3 showed promising results, but due to stress it is also a bit inclined as shown in Figure 56.

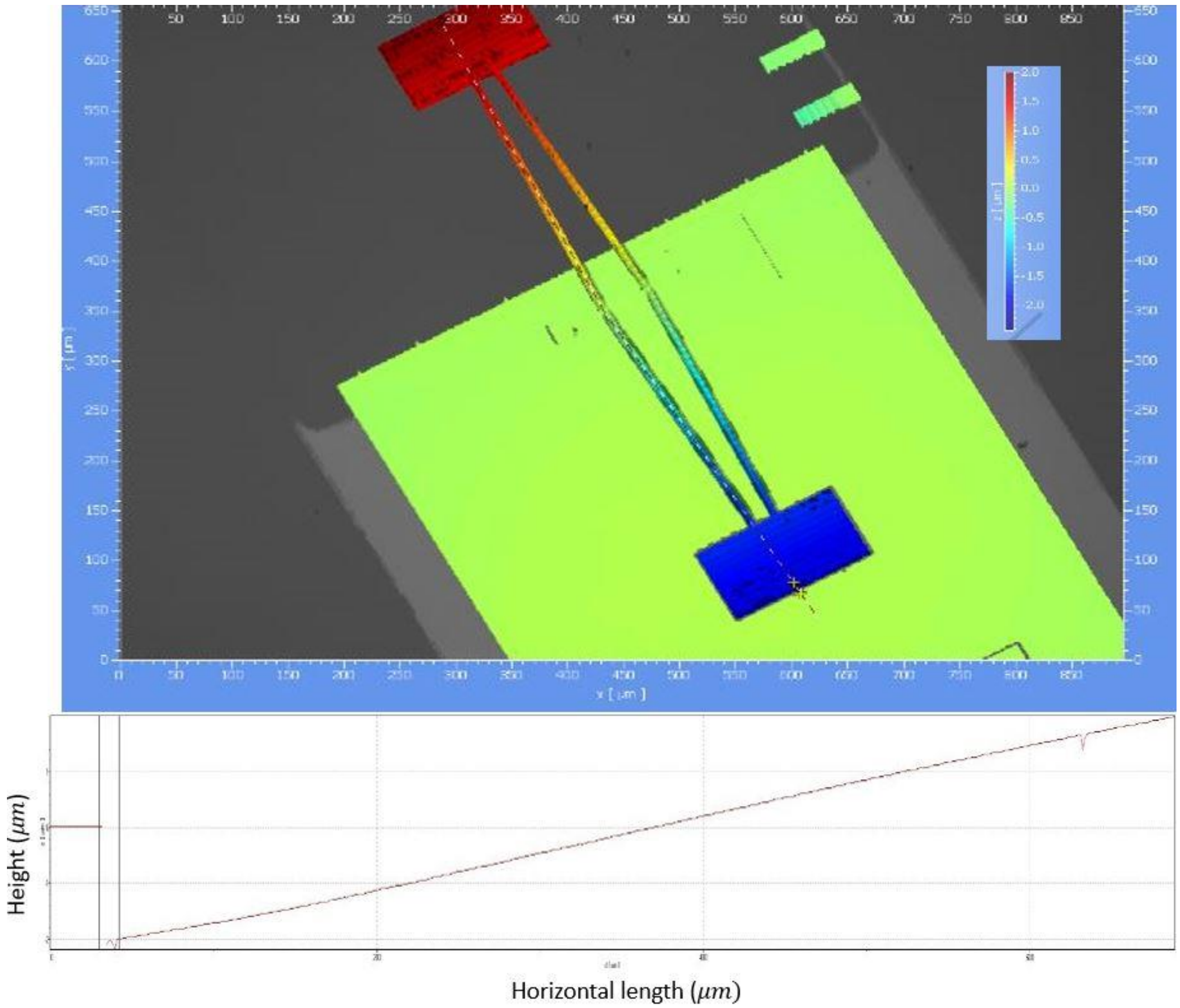

Figure 55: White light interfernce results for sample2

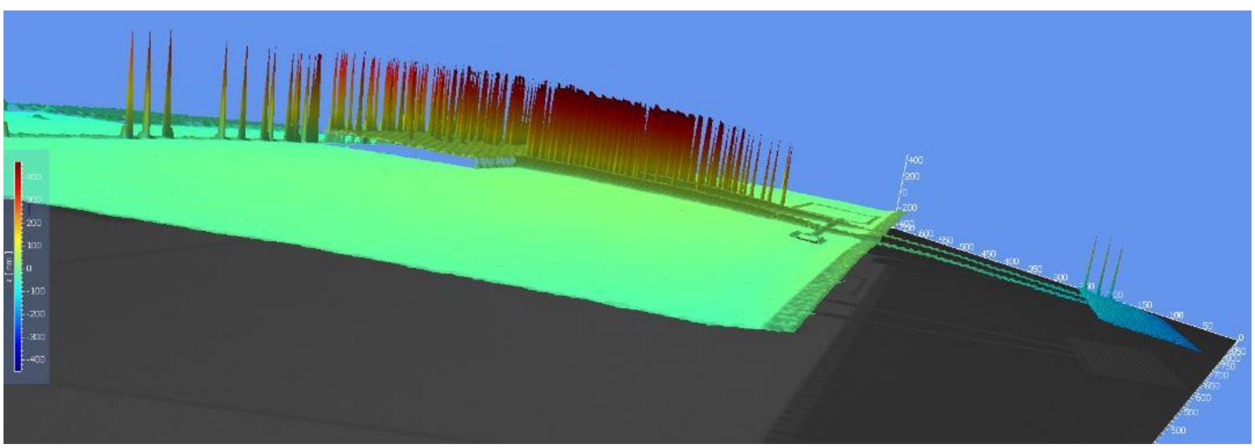

Figure 56: White light interfernce results for sample3

The pull-in voltage measurements for of sample3 is taken by applying a dc bias with overlapping ac signal of 100mv. The device stop responding after crossing 2V of dc bias. Hence the pull-in voltage measured is 2V. The reason for high pull-in voltage could be the stress in the device due to which it is bent upwards, which increases the distance between the substrate and the paddle. Thus, requires more voltage to pull the plate. Incorporating the increased distance ($d_0 = 3$) between the plate and the substrate, the pull-in voltage can be calculated by the equation *3.26*. as 1.5 V. Still, there is error of about 25 % in measured and calculated value. More samples need to be measurements to come to a better conclusion about pull-in voltage.

Chapter 5: Conclusion and Recommendations

Flow sensors to study the airflow close to plants leaf are investigated including thermal flow sensors, skin friction sensors and, drag force sensors. Thermal sensors are not recommended because of high possibility of leaves acting as a heat sink which may reduce the accuracy of results, whereas the skin friction sensors have large size, thus, would obstruct the flow. Drag force sensor have been recommended as it is suitable for the measurement near leaf i.e cantilever based drag force sensor can be mounted probe which would put least effect on the flow near the leaf. Moreover, high sensitivity and ease of fabrication using MEMS- based technology are advantages in favour.

To meet the application requirements, drag force sensor based on capacitive readout is designed and simulated in COMSOL Multiphyiscs 5.5, for maximum airflow of 1m/s. Using simulations, effect of various parameter on the defection and mode frequencies of the sensor has been investigated to pave the way to find the optimum combination of parameters. The maximum deflection depends on the effective length of the spring (given width and thickness is constant). A slight increase θ can significantly reduce the sideways movement in y-direction. Same can also be achieved by increasing the thickness of the cantilever beams. Cantilever beams could be unpredictable at width lower than 16 μm. Maximum deflection of 0.632 μm with plate side of 400 μm could give change in capacitance of more than 200 fF.

Detailed study on calculating torsional spring constant has been presented. Different approaches and error associated with each approach have been investigated to give clarity on torsional spring for future designs and fellow researchers. The pull- in voltage of the device is very low, makes it difficult to use capacitance conversion chips like AD7747 which works on minimum voltage of 2.7 V. Couple of designs to increase the pull-in voltage are recommended in section 3.8 for future designs. The stress in the device is 2MPa which implies that the device can be improved further or made more sensitive. The width of the torsion spring (4 μm) is limited by minimum feature size in the fabrication process.

The device is succesfully fabricated using MEMS-based technology in MESA^+ lab at University of Twente. A few samples are analzed using white light interference and pull-in voltage for one the samples is measured to be 2.0 V. More samples need to be tested to come to a better conclusion about pull-in voltage. A test setup has been made to obatin the velocity profile inside the a hollow tube filled with straws using anemometer sensor. The obtained velocity profile can be used to characterize the fabricated flow sensor.

Chapter 6: References

[1] “What is Horticulture? A Modern Applied Plant Science! - Department of Horticulture.” [Online]. Available: https://www.canr.msu.edu/hrt/about-us/horticulture_is. [Accessed: 18-Dec-2020].

[2] “What is Horticulture? - ASHS.” [Online]. Available: https://ashs.org/page/Horticulture. [Accessed: 18-Dec-2020].

[3] “Horticultural exports down in April 2020.” [Online]. Available: https://www-cbs-nl.ezproxy2.utwente.nl/en-gb/news/2020/26/horticultural-exports-down-in-april-2020. [Accessed: 24-Dec-2020].

[4] “The Greenhouse Pharmacy - WUR.” [Online]. Available: https://www.wur.nl/en/newsarticle/Greenhouse-pharmacy-greenhouse-horticulture.htm. [Accessed: 22-Dec-2020].

[5] R. R. Shamshiri, J. W. Jones, K. R. Thorp, D. Ahmad, H. C. Man, and S. Taheri, “Review of optimum temperature, humidity, and vapour pressure deficit for microclimate evaluation and control in greenhouse cultivation of tomato: A review,” *International Agrophysics*, vol. 32, no. 2. Walter de Gruyter GmbH, pp. 287–302, 01-Apr-2018, doi: 10.1515/intag-2017-0005.

[6] A. López, D. L. Valera, F. D. Molina-Aiz, and A. Peña, “Effectiveness of horizontal air flow fans supporting natural ventilation in a Mediterranean multi-span greenhouse,” *Sci. Agric.*, vol. 70, no. 4, pp. 219–228, Jul. 2013, doi: 10.1590/S0103-90162013000400001.

[7] “Horizontal Air Flow Systems - CT Integrated Pest Management Program.” [Online]. Available: http://ipm.uconn.edu/documents/raw2/Horizontal Air Flow Systems/Horizontal Air Flow Systems.php?aid=221. [Accessed: 10-Jan-2021].

[8] “Greenhouse & Floriculture: Horizontal Air Flow is Best for Greenhouse Air Circulation | UMass Center for Agriculture, Food and the Environment.” [Online].

Available: https://ag.umass.edu/greenhouse-floriculture/fact-sheets/horizontal-air-flow-is-best-for-greenhouse-air-circulation. [Accessed: 10-Jan-2021].

[9] S. G. Pallardy, "Transpiration and Plant Water Balance," in *Physiology of Woody Plants*, Elsevier, 2008, pp. 325–366.

[10] G. S. Campbell and J. M. Norman, "The description and measurement of plant canopy structure," *Plant canopies*, pp. 1–19, 1990, doi: 10.1017/cbo9780511752308.002.

[11] M. W. Moffett, "What's 'Up'? A Critical Look at the Basic Terms of Canopy Biology1," *Biotropica*, vol. 32, no. 4, p. 569, Dec. 2000, doi: 10.1646/0006-3606(2000)032[0569:wsuacl]2.0.co;2.

[12] H. Schlichting, *Boundary layer theory*. 1968.

[13] "The Boundary Layer and Its Importance - Greenhouse Product News." [Online]. Available: https://gpnmag.com/article/the-boundary-layer-and-its-importance/. [Accessed: 21-Dec-2020].

[14] "Vision and mission - 4TU.Federation." [Online]. Available: https://www.4tu.nl/plantenna/en/Plantenna_Intro/. [Accessed: 21-Dec-2020].

[15] O. Sazhin, "Liquid flow meter based on a thermal anemometer microsensor," *J. Appl. Fluid Mech.*, vol. 9, no. 5, pp. 1735–3645, 1991, doi: 10.18869/acadpub.jafm.68.235.24600.

[16] F. Ejeian *et al.*, "Design and applications of MEMS flow sensors: A review," *Sensors and Actuators, A: Physical*, vol. 295. Elsevier B.V., pp. 483–502, 15-Aug-2019, doi: 10.1016/j.sna.2019.06.020.

[17] J. T. W. Kuo, L. Yu, and E. Meng, "Micromachined thermal flow sensors-A review," *Micromachines*, vol. 3, no. 3, pp. 550–573, 2012, doi: 10.3390/mi3030550.

[18] "XII. On the convection of heat from small cylinders in a stream of fluid: Determination of the convection constants of small platinum wires with applications to hot-wire anemometry," *Philos. Trans. R. Soc. London. Ser. A, Contain. Pap. a*

Math. or Phys. Character, vol. 214, no. 509–522, pp. 373–432, Jan. 1914, doi: 10.1098/rsta.1914.0023.

[19] "HOT-WIRE AND HOT-FILM ANEMOMETRY."

[20] E. Meng, "MEMS TECHNOLOGY AND DEVICES FOR A MICRO FLUID DOSING SYSTEM," 2003.

[21] H. H. Bruun, "Hot-Wire Anemometry: Principles and Signal Analysis," *Meas. Sci. Technol.*, vol. 7, no. 10, Oct. 1996, doi: 10.1088/0957-0233/7/10/024.

[22] J. Groenesteijn, "Microfluidic platform for Coriolis-based sensor and actuator systems," University of Twente, Enschede, The Netherlands, 2016.

[23] M. Elwenspoek and R. Wiegerink, "Flow Sensors," 2001, pp. 153–208.

[24] T. S. J. Lammerink, N. R. Tas, M. Elwenspoek, and J. H. J. Fluitman, "Micro-liquid flow sensor," *Sensors Actuators A. Phys.*, vol. 37–38, no. C, pp. 45–50, Jun. 1993, doi: 10.1016/0924-4247(93)80010-E.

[25] H. Ernst, A. Jachimowicz, and G. A. Urban, "High resolution flow characterization in Bio-MEMS," *Sensors Actuators, A Phys.*, vol. 100, no. 1, pp. 54–62, Aug. 2002, doi: 10.1016/S0924-4247(02)00187-5.

[26] T. S. J. Lammerink, N. R. Tas, G. J. M. Krijnen, and M. Elwenspoek, "New class of thermal flow sensors using ΔT = 0 as a control signal," *Proc. IEEE Micro Electro Mech. Syst.*, pp. 525–530, 2000, doi: 10.1109/memsys.2000.838572.

[27] J. van Kuijk, T. S. J. Lammerink, H. E. de Bree, M. Elwenspoek, and J. H. J. Fluitman, "Multi-parameter detection in fluid flows," *"Sensors Actuators, A Phys.*, vol. 47, no. 1–3, pp. 369–372, 1995, doi: 10.1016/0924-4247(94)00923-6.

[28] B. Yu, Z. Gan, S. Cao, J. Xu, and S. Liu, "A micro channel integrated gas flow sensor for high sensitivity," in *2008 11th IEEE Intersociety Conference on Thermal and Thermomechanical Phenomena in Electronic Systems, I-THERM*, 2008, pp. 215–220, doi: 10.1109/ITHERM.2008.4544273.

[29] G. Kaltsas and A. G. Nassiopoulou, "Novel C-MOS compatible monolithic silicon

gas flow sensor with porous silicon thermal isolation," *Sensors Actuators, A Phys.*, vol. 76, no. 1–3, pp. 133–138, Aug. 1999, doi: 10.1016/S0924-4247(98)00370-7.

[30] V. Balakrishnan, T. Dinh, H. P. Phan, D. V. Dao, and N. T. Nguyen, "Highly sensitive 3C-SiC on glass based thermal flow sensor realized using MEMS technology," *Sensors Actuators, A Phys.*, vol. 279, pp. 293–305, Aug. 2018, doi: 10.1016/j.sna.2018.06.025.

[31] B. Idjeri, M. Laghrouche, and J. Boussey, "Wind Measurement Based on MEMS Micro-Anemometer with High Accuracy Using ANN Technique," *IEEE Sens. J.*, vol. 17, no. 13, pp. 4181–4188, Jul. 2017, doi: 10.1109/JSEN.2017.2701502.

[32] J. J. Miau, J. K. Tu, J. H. Chou, and G. B. Lee, "Sensing flow separation on a circular cylinder by micro-electrical- mechanical-system thermal-film sensors," *AIAA J.*, vol. 44, no. 10, pp. 2224–2230, Oct. 2006, doi: 10.2514/1.17408.

[33] M. M. Sadeghi, R. L. Peterson, and K. Najafi, "Air flow sensing using micro-wire-bonded hair-like hot-wire anemometry," *J. Micromechanics Microengineering*, vol. 23, no. 8, pp. 85017–85028, Aug. 2013, doi: 10.1088/0960-1317/23/8/085017.

[34] S. Kim, T. Nam, and S. Park, "Measurement of flow direction and velocity using a micromachined flow sensor," *Sensors Actuators, A Phys.*, vol. 114, no. 2–3, pp. 312–318, Sep. 2004, doi: 10.1016/j.sna.2003.12.019.

[35] A. Padmanabhan, H. Goldberg, K. D. Breuer, and M. A. Schmidt, "A wafer-bonded floating-element shear stress microsensor with optical position sensing by photodiodes," *J. Microelectromechanical Syst.*, vol. 5, no. 4, pp. 307–315, 1996, doi: 10.1109/84.546410.

[36] M. Elwenspoek and R. Wiegerink, *Mechanical Microsensors*. Berlin, Heidelberg: Springer Berlin Heidelberg, 2001.

[37] J. Zhe, K. R. Farmer, and V. Modi, "A MEMS device for measurement of skin friction with capacitive sensing," *2001 Microelectromechanical Syst. Conf. MEMS 2001*, pp. 4–7, 2002, doi: 10.1109/MEMSC.2001.992728.

[38] M. Sheplak, L. Cattafesta, T. Nishida, and C. B. McGinley, "MEMS Shear Stress

Sensors: Promise and Progress. 24th AIAA Aerodynamic Meas," *Tech. Gr. Test. Conf. AIAA*, pp. 1–13, 2004.

[39] "What is Drag?" [Online]. Available: https://www.grc.nasa.gov/www/k-12/airplane/drag1.html. [Accessed: 06-Jan-2021].

[40] "An Introduction to Fluid Dynamics - G. K. Batchelor - Google Books." [Online]. Available: https://books.google.ca/books?id=aXQgAwAAQBAJ. [Accessed: 06-Jan-2021].

[41] "The Drag Coefficient." [Online]. Available: https://www.grc.nasa.gov/www/k-12/airplane/dragco.html. [Accessed: 06-Jan-2021].

[42] D. F. Young, B. R. Munson, T. H. Okiishi, and W. W. Huebsch, *A Brief Introduction to Fluid Mechanics*, 5th ed. John Wiley & Sons, 2010.

[43] A. M. K. Dagamseh, C. M. Bruinink, H. Droogendijk, R. J. Wiegerink, T. S. J. Lammerink, and G. J. M. Krijnen, "Engineering of biomimetic hair-flow sensor arrays dedicated to high-resolution flow field measurements," *Proc. IEEE Sensors*, pp. 2251–2254, 2010, doi: 10.1109/ICSENS.2010.5690705.

[44] Z. Fan, J. Chen, J. Zou, D. Bullen, C. Liu, and F. Delcomyn, "Design and fabrication of artificial lateral line flow sensors," 2002.

[45] Y. Ozaki, T. Ohyama, T. Yasuda, and I. Shimoyama, "Air flow sensor modeled on wind receptor hairs of insects," *Proc. IEEE Micro Electro Mech. Syst.*, pp. 531–536, 2000, doi: 10.1109/memsys.2000.838573.

[46] T. Lammerink, "Fabrication of arrays of artificial hairs for complex flow pattern recognition." .

[47] M. Dijkstra, J. J. Van Baar, R. J. Wiegerink, T. S. J. Lammerink, J. H. De Boer, and G. J. M. Krijnen, "Artificial sensory hairs based on the flow sensitive receptor hairs of crickets," *J. Micromechanics Microengineering*, vol. 15, no. 7, p. S132, Jul. 2005, doi: 10.1088/0960-1317/15/7/019.

[48] G. J. M. Krijnen *et al.*, "MEMS based hair flow-sensors as model systems for

acoustic perception studies," *Nanotechnology*, vol. 17, no. 4, pp. S84–S89, Feb. 2006, doi: 10.1088/0957-4484/17/4/013.

[49] C. M. Bruinink *et al.*, "Advancement in tecnology and design of biomimetic flow-Sensor arrays," in *Proceedings of the IEEE International Conference on Micro Electro Mechanical Systems (MEMS)*, 2009, pp. 152–155, doi: 10.1109/MEMSYS.2009.4805341.

[50] G. Krijnen, T. Lammerink, and R. Wiegerink, "Cricket Inspired Flow-Sensor Arrays."

[51] Y. H. Wang, C. Y. Lee, and C. M. Chiang, "A MEMS-based air flow sensor with a free-standing microcantilever structure," *Sensors*, vol. 7, no. 10, pp. 2389–2401, 2007, doi: 10.3390/s7102389.

[52] L. Du, Z. Zhao, C. Pang, and Z. Fang, "Drag force micro solid state silicon plate wind velocity sensor," *Sensors Actuators, A Phys.*, vol. 151, no. 1, pp. 35–41, 2009, doi: 10.1016/j.sna.2009.02.003.

[53] Y. Su, A. G. R. Evans, A. Brunnschweiler, and G. Ensell, "Characterization of a highly sensitive ultra-thin piezoresistive silicon cantilever probe and its application in gas flow velocity sensing," *J. Micromechanics Microengineering*, vol. 12, no. 6, pp. 780–785, 2002, doi: 10.1088/0960-1317/12/6/309.

[54] I. S. Devised *et al.*, "Process Document MEMS," *Ultrasound*, no. 19121130, 2011.

[55] "(No Title)." [Online]. Available: https://wp.optics.arizona.edu/optomech/wp-content/uploads/sites/53/2016/10/OPTI_222_W13.pdf. [Accessed: 15-Jan-2021].

[56] W. C. Young and R. G. Budynas, *Elastic stability*, vol. 4, no. C. 1980.

[57] "What is Von Mises Stress? | SimScale Finite Element Analysis." [Online]. Available: https://www.simscale.com/docs/simwiki/fea-finite-element-analysis/what-is-von-mises-stress/. [Accessed: 24-Jan-2021].

[58] Z. Zhang, P. Chen, F. Qin, T. An, and H. Yu, "Mechanical properties of silicon in subsurface damage layer from nano-grinding studied by atomistic simulation ARTICLES YOU MAY BE INTERESTED IN Mechanical properties of silicon in

subsurface damage layer from nano-grinding studied by atomistic simulation," *AIP Adv.*, vol. 8, p. 55223, 2018, doi: 10.1063/1.5021654.

[59] "Course of Theoretical Physics Vol 7: Theory of Elasticity - Lev Davidovich Landau, E. M. Lifshitz - Google Books." [Online]. Available: https://books.google.nl/books/about/Course_of_Theoretical_Physics_Vol_7.html?id=pVfltAEACAAJ&redir_esc=y. [Accessed: 24-Jan-2021].

[60] E. L. C. Ng and K. T. Z. Oo, "CMOS Torsional Micromirror," pp. 2–5.

[61] C. P. Green, H. Lioe, J. P. Cleveland, R. Proksch, P. Mulvaney, and J. E. Sader, "Normal and torsional spring constants of atomic force microscope cantilevers," *Rev. Sci. Instrum.*, vol. 75, no. 6, pp. 1988–1996, 2004, doi: 10.1063/1.1753100.

[62] D. Kwak, J. Kim, S. Park, H. Ko, and D. Il Cho, "Why is (111) silicon a better mechanical material for MEMS: Torsion case," *Am. Soc. Mech. Eng. Micro-Electromechanical Syst. Div. Publ.*, vol. 5, no. 111, pp. 259–264, 2003, doi: 10.1115/imece2003-41869.

[63] "Polar Moment of Inertia - ExtruDesign." [Online]. Available: https://extrudesign.com/polar-moment-of-inertia/. [Accessed: 24-Jan-2021].

[64] "INTRODUCTION TO MECHANICS AND TRANSDUCER," no. October, 2019.

[65] P. Tongpun, E. Bumrungthaichaichan, and S. Wattananusorn, "Investigation of entrance length in circular and noncircular conduits by computational fluid dynamics simulation."

[66] G. Lake-Bakaar, M. Ahmed, A. Evenson, A. Bonder, S. Faintuch, and V. Sundaram, "Hagen-Poiseuille's law: The link between cirrhosis, liver stiffness, portal hypertension and hepatic decompensation," *World J. Hepatol.*, vol. 7, no. 1, pp. 28–32, 2015, doi: 10.4254/wjh.v7.i1.28.